

Label-free imaging of M1 and M2 macrophage phenotypes in the human dermis in vivo using two-photon excited FLIM

Marius Kröger¹, Jörg Scheffel¹, Evgeny A Shirshin², Johannes Schleusener¹, Martina C Meinke¹, Jürgen Lademann¹, Marcus Maurer¹, Maxim E Darwin^{1*}

¹Charité – Universitätsmedizin Berlin, corporate member of Freie Universität Berlin, Humboldt- Universität zu Berlin, and Berlin Institute of Health, Department of Dermatology, Venerology and Allergology, Berlin, Germany; ²Lomonosov Moscow State University, Faculty of Physics, Moscow, Russian Federation

Abstract Macrophages (MΦs) are important immune effector cells that promote (M1 MΦs) or inhibit (M2 MΦs) inflammation and are involved in numerous physiological and pathogenic immune responses. Their precise role and relevance, however, are not fully understood for lack of noninvasive quantification methods. Here, we show that two-photon excited fluorescence lifetime imaging (TPE-FLIM), a label-free noninvasive method, can visualize MΦs in the human dermis in vivo. We demonstrate in vitro that human dermal MΦs exhibit specific TPE-FLIM properties that distinguish them from the main components of the extracellular matrix and other dermal cells. We visualized MΦs, their phenotypes and phagocytosis in the skin of healthy individuals in vivo using TPE-FLIM. Additionally, machine learning identified M1 and M2 MΦs with a sensitivity of 0.88 ± 0.04 and 0.82 ± 0.03 and a specificity of 0.89 ± 0.03 and 0.90 ± 0.03 , respectively. In clinical research, TPE-FLIM can advance the understanding of the role of MΦs in health and disease.

*For correspondence: maxim.darwin@protonmail.com

Competing interest: The authors declare that no competing interests exist.

Funding: See page 17

Preprinted: 30 November 2021

Received: 05 August 2021

Accepted: 05 October 2022

Published: 06 October 2022

Reviewing Editor: Michael L Dustin, University of Oxford, United Kingdom

© Copyright Kröger et al. This article is distributed under the terms of the [Creative Commons Attribution License](https://creativecommons.org/licenses/by/4.0/), which permits unrestricted use and redistribution provided that the original author and source are credited.

Editor's evaluation

The authors have used measurements of endogenous fluorescence lifetimes in the two-photon stimulated NAD(P)H excitation-emission range to build an in vivo classifying for macrophage differentiation status in human dermis. The training data was derived from in vitro and ex vivo analysis of M1 and M2 polarised macrophages from peripheral blood, isolated from tissue or studies ex vivo in frozen sections with marker based validation. A machine learning approach for in vivo classification is presented and an approach to detect phagocytes in vivo is suggested.

Introduction

Macrophages (MΦs) are important immune effector cells in organs and tissues that act as border junctions to environments such as the gut, the airways, and the skin (*Elhelu, 1983*). Skin MΦs (*Dong et al., 2016; Estandarte et al., 2016; Rytter, 1985*) originate from circulating monocytes (*Geissmann et al., 2010; Gordon and Taylor, 2005*) via the same infiltration route into the dermis as monocyte-derived dendritic cells (*Schmid and Harris, 2014; Figure 1a*) and are mainly located in the papillary and reticular dermis in close proximity to blood vessels (*Weber-Matthiesen and Sterry, 1990; Figure 1b–d*). It has been known for more than 30 years that skin MΦs are abundant and heterogeneous, based on their morphology, localization, and staining properties (*Weber-Matthiesen and*

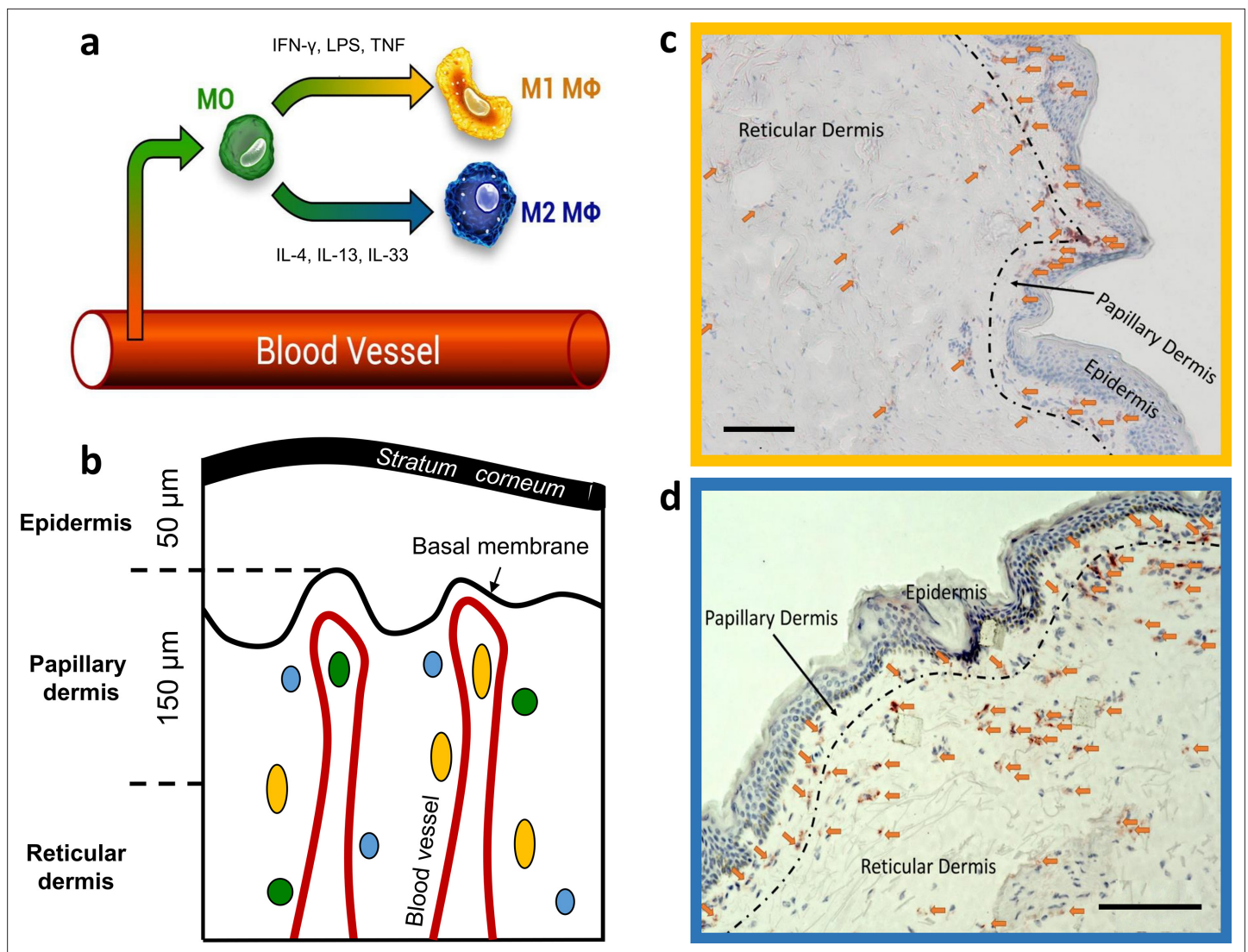


Figure 1. Dermal monocyte skin infiltration and CD68 stained M1 and CD163 stained M2 MΦs distribution in excised human skin. Schematic illustration of monocyte (MO) (green) infiltration into tissues and macrophage (MΦ)-polarization into M1 MΦs (yellow) via IFN- γ , LPS, and TNF and M2 MΦs (blue) via IL-4, IL-13, and IL-33 (a). Schematic of skin with exemplary locations of monocytes (green), M1 MΦs (yellow), and M2 MΦs (blue) (b). Density of M1 MΦs (marked with arrows) stained with CD68 (c) and M2 MΦs (marked with arrows) stained with CD163 (d) in 10 μ m thick cryo-section. Scale bar: 100 μ m. The terms M1 and M2 MΦs are simplistic, as many signals modulate MΦ functions, resulting in a spectrum between the M1 and M2 MΦ phenotypes.

Sterry, 1990). More recently, skin MΦs have been classified based on their function, and they fall into two phenotypes referred to as inflammation-promoting M1-polarised MΦs (classically activated) and anti-inflammatory M2-polarised MΦs (alternatively activated) (**Arango Duque and Descoteaux, 2014; Figure 1a**). M1 MΦs are activated by viral and bacterial infection (**Benoit et al., 2008; Ferrer et al., 2019; Malmgaard et al., 2004**), interferon- γ , lipopolysaccharide (LPS), and tumor necrosis factor (TNF), which is known as the classical activation pathway (**Li and Liu, 2018**). M2 MΦs are alternatively activated in response to IL-4, IL-13, and IL-33 (**Furukawa et al., 2017; Sica and Mantovani, 2012**). Recently, this paradigm was questioned, as a manifold of cytokines, biomarkers, and activators are involved in MΦs functioning, resulting in a continuum of states between the M1 and M2 phenotypes (**Mendoza-Coronel and Ortega, 2017; Murray et al., 2014**). Furthermore, different markers like CXCL10 for M1 MΦs and CCL17 for M2 MΦs can have the function to attract t-cells. Macrophages in disease, cancer, or obesity can switch function from wound healing to inflammatory MΦs

given the right signals and microenvironment (*Mosser and Edwards, 2008*). However, for simplicity, the terms M1 and M2 MΦs are used here with the activators in brackets, where applicable.

Skin M1 MΦs are held to contribute to dermal innate immunity and homeostasis. This is supported by reports that M1 MΦs can phagocytose objects up to 20 μm in size (*Morhenn et al., 2002*), promote skin inflammatory and immune responses (*Remmerie and Scott, 2018; Theret et al., 2019; Yanez et al., 2017*), and produce nitric oxide and other reactive oxygen species (ROS) (*Forman and Torres, 2001; Rendra et al., 2019*). Skin M2 MΦs, on the other hand, are thought to promote dermal repair, healing, and regeneration, for example, by contributing to the formation of the extracellular matrix (ECM; *Ploeger et al., 2013*).

The precise role of skin MΦs and their M1 and M2 phenotypes in health and disease remain to be elucidated. In skin diseases, such as melanoma (*Bardi et al., 2018*), systemic sclerosis (*Trombetta et al., 2018*), Lupus (*Chong et al., 2015*), and LPS tolerance (*O'Carroll et al., 2014*), polarization of MΦs leading to mixed M1 and M2 phenotypes can be observed. It is not known whether and in what density mixed MΦ phenotypes are to be expected in healthy skin. The fluorescence properties of mixed phenotypes have not been studied.

Efforts to do so include their quantification in healthy human skin and in lesional and nonlesional skin of patients with skin diseases. Currently, the most common approach is to obtain skin biopsies and to visualize MΦs by immunohistochemistry. Skin biopsies, however, come with several important limitations, which include scarring, the risk of infection and bleeding, and artificial findings caused by the use of local anesthesia. In addition, histopathological analyses of skin biopsies are not well suited for characterizing MΦ functions such as phagocytosis and for long-term monitoring of MΦ distribution in the skin.

Fluorescence lifetime imaging (FLIM) employs NAD(P)H and fluorescence decay parameters of cellular compartments as specific indicators of cell types and phenotypes (*Alfonso-García et al., 2016; Heaster et al., 2021*). Combined with two-photon tomography, two-photon excited fluorescence lifetime imaging (TPE-FLIM) allows for label-free and noninvasive imaging of dermal cells. For instance, TPE-FLIM allows for in vitro imaging of mast cells, fibroblasts, neutrophils, and dendritic cells and in vivo imaging of mast cells in human skin (*Kröger et al., 2020*). Whether or not TPE-FLIM can be used to visualize human skin MΦs, their M1 and M2 phenotypes, and their functions, is currently unknown. There are, however, several independent lines of evidence that support this approach: First, previous studies have shown that TPE-FLIM can distinguish MΦs from other dermal cells and ECM, without prior labeling (*Kröger et al., 2020*). Second, the capillaries of the papillary dermis, which often are in close proximity to MΦs, show distinct TPE-FLIM signatures and are readily visualized (*Shirshin et al., 2017*). Third, M1 and M2 MΦs come with unique cytokine patterns, and the TPE-FLIM signatures of these cytokines and patterns could help to tell the two phenotypes apart. Finally, TPE-FLIM can distinguish between functional states of dermal cells, for example, resting and activated mast cells in vivo, MΦs ex vivo (*Kröger et al., 2020*), and T-cell activation in vitro (*Walsh et al., 2021*) may, therefore, potentially allow for monitoring MΦ functions in vivo (*Szulcowski et al., 2016*). Taken together, the morphological features of skin MΦs, their localization in the skin, and the expected differences in fluorescence decay parameters between MΦ phenotypes as well as between other dermal cells, make TPE-FLIM a promising strategy for their detection (*Yakimov et al., 2019*).

Here, we first investigated human skin MΦs, in vitro with clear M1 and M2 phenotypes, for their TPE-FLIM properties and how these differ from those of the main components of the ECM and other dermal cells such as fibroblasts, mast cells, and dendritic cells. We then applied the identified MΦ TPE-FLIM signatures to investigate M1 and M2 MΦs and their phenotypes in human skin biopsies, combined with traditional immunohistochemistry-based visualization. Finally, we used TPE-FLIM in vivo in humans to study skin MΦs, their phenotypes, and functions, and we developed, tested, and characterized TPE-FLIM signature-based machine learning algorithms for the detection of skin MΦs.

Results

In vitro monocyte-derived M1 and M2 MΦs show distinct TPE-FLIM parameters

The TPE-FLIM images of monocytes isolated from human peripheral blood mononuclear cells (PBMCs) showed a round morphology (diameter of up to 10 μm) with a barely visible nucleus, homogeneously

distributed cell content, and regular borders with no membrane extensions (**Figure 2—figure supplement 1**). M Φ s differentiated from PBMC and polarised toward M1 M Φ s with interferon- γ (IFN- γ ; $n=21$) and toward M2 M Φ s with interleukin-4 (IL-4; $n=27$) were similar in size, ranging 10–12 μm (**Figure 2a–c**). M1 and M2 M Φ s showed comparable overall TPE-AF intensities, but they differed significantly in several other features. M1 M Φ s also showed numerous bright spots (typical size is 2–3 μm), likely vacuoles and mitochondria, had less visible borders, and exhibited higher TPE-AF intensity than M2 M Φ s. In contrast, M2 M Φ s were characterized by distinct borders with filopodia (**Figure 2b**; **Figure 2—figure supplement 2**), which were rarely seen in M1 M Φ s (**Figure 2a**).

M1 and M2 M Φ s also differed in their TPE-FLIM parameters τ_1 , τ_2 , and τ_m (**Figure 2d**). TPE-AF decay times were significantly shorter in M1 M Φ s ($n=21$) than in M2 M Φ s ($n=27$; $p<0.05$), and both M Φ s differed significantly, in their TPE-FLIM parameters, from monocytes ($n=15$; $p<0.05$; **Table 1**).

IgG stimulation of IgG immune complex-sensitized M1 and M2 M Φ s resulted in the release of inflammatory mediators, but did not lead to significant changes or reveal additional differences in TPE-FLIM parameters 2 and 5 days after differentiation of PBMC into M Φ s (data not shown). Taken together, these findings indicate that monocyte-derived M1 M Φ s and M2 M Φ s can be identified and distinguished in vitro by their distinct TPE-FLIM signatures.

M Φ s isolated from periorcular skin show TPE-FLIM parameters that are similar to those of in vitro monocyte-derived M1 M Φ s or M2 M Φ s

Human M Φ s isolated from periorcular skin and analyzed by immunohistochemistry were irregularly shaped, with poorly defined borders, 8–10 μm in size, pericentral nuclei of 5–6 μm diameter with low fluorescence intensity, heterogeneously and irregularly distributed cellular content, and they exhibited a bright fluorescence multivacuolated cytoplasm with ≈ 1 μm diameter small bright spots, presumably related to mitochondria and/or vacuoles (**Figure 2c**). Based on their TPE-FLIM parameters, dermal M Φ s fell into two significantly different groups (**Figure 2d**): group 1 ($n=34$), with stronger TPE-AF intensity ($\approx 3000 \pm 500$ photons/mW) and shorter lifetimes, and group 2 ($n=28$), with a weaker TPE-AF intensity ($\approx 800 \pm 200$ photons/mW) with longer lifetimes (**Figure 2c**; **Figure 2—figure supplement 3**). The profiles of dermal M Φ s in groups 1 and 2 were similar to those of monocyte-derived M1 M Φ s and M2 M Φ s, respectively (**Figure 2d**; **Table 1**). The biggest differences between group 1/M1 M Φ s and group 2/M2 M Φ s were shorter τ_1 and τ_m as well as larger size (10.9 ± 0.6 μm) in the former as compared to the latter (9.8 ± 1.2 μm ; $p<0.05$; **Figure 2c and d**; **Table 1**). This suggests that human skin M Φ s, based on their in vitro TPE-FLIM signatures, can be assigned to one of two phenotypes, where the first is similar to that of monocyte-derived M1 M Φ s and the second is similar to that of monocyte-derived M2 M Φ s.

It should be noted that the TPE-FLIM parameters were stable over the measurements that took up to 1 hr for in vitro M1 and M2 M Φ s isolated from periorcular skin (**Figure 2—figure supplement 4**). Their TPE-FLIM values vary within the standard deviation shown in **Table 1**.

TPE-FLIM can distinguish between M Φ s and other cells

To prove that the recorded TPE-FLIM signatures are unique for M1- and M2-polarized M Φ s (**Figure 2**), we performed TPE-FLIM measurements of other dermal cells in vitro, such as mast cells, dendritic cells, fibroblasts, monocytes, and neutrophils. Their TPE-FLIM parameters, summarized in **Table 1**, are markedly different from those of the established signatures of M1- and M2-polarized M Φ s. Thus, in addition to size, morphology, and internal vacuole structure, M1- and M2-polarized M Φ s can be distinguished, from each other and other cells, by distinct TPE-FLIM parameters, a prerequisite for the visualization of skin M Φ s ex vivo and in vivo. **Table 1** is an extension of the results shown in Kröger *et al.*, 2020.

Immunohistochemistry confirms TPE-FLIM detection of M1 and M2 M Φ s in human skin ex vivo

To test if the TPE-FLIM signatures established in vitro identify M1- and M2-polarized M Φ s in human skin, we sequentially analyzed dermal biopsies by TPE-FLIM and conventional immunohistochemistry. The application of in vitro M Φ signatures to TPE-FLIM analyses of 13 human skin biopsy cryo-sections identified two distinct cell populations: The first showed a short mean fluorescence lifetime τ_m and high TPE-AF intensity, a feature of M1 M Φ s (**Table 1**, **Figure 2d**, **Figure 3a**); the second population

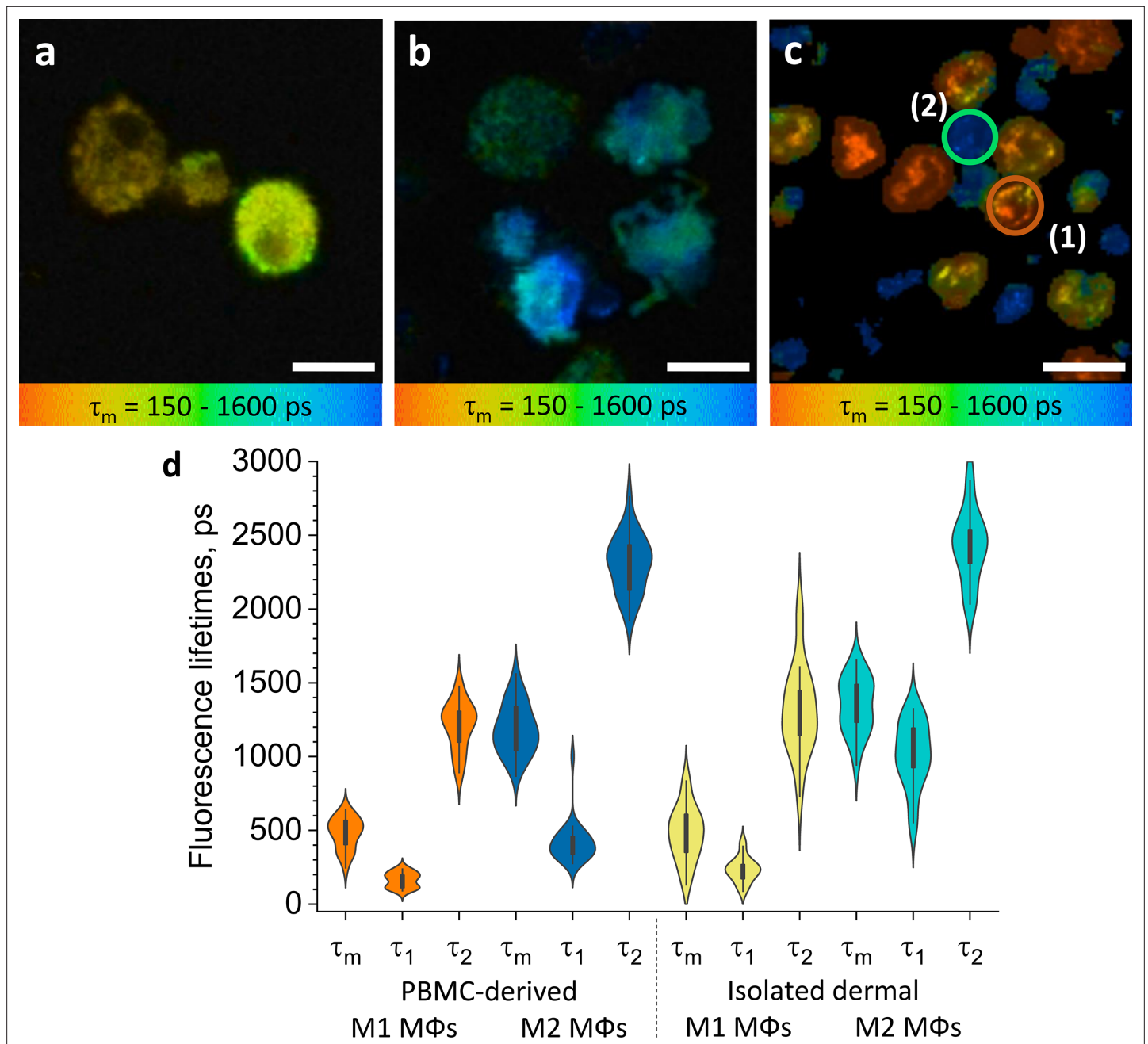


Figure 2. M Φ s polarised from PBMC and isolated dermal M Φ s show distinct TPE-FLIM signatures. TPE-FLIM τ_m images (mean fluorescence lifetime τ_m in the 150–1600 ps range) of monocyte-derived M1-polarised (IFN- γ) M Φ s (**a**), monocyte-derived M2-polarised (IL-4) M Φ s (**b**), and isolated human dermal M1 M Φ s (1) and M2 M Φ s (2) (**c**). Scale bar: 10 μ m. The distribution of TPE-FLIM parameters τ_1 , τ_2 , and τ_m for monocyte-derived M1-polarised M Φ s ($n=21$, orange), M2-polarised M Φ s ($n=27$, dark blue), and isolated dermal M1 M Φ s ($n=34$, yellow), M2 M Φ s ($n=28$, light blue) (**d**). The boxplot represents 25–75% of the values. PBMC, peripheral blood mononuclear cell; TPE-FLIM, two-photon excited fluorescence lifetime imaging.

The online version of this article includes the following figure supplement(s) for figure 2:

Figure supplement 1. TPE-FLIM visualization of PBMC and histogram of TPE-FLIM parameter.

Figure supplement 2. In vitro 2D segmentation for M Φ s from PBMC.

Figure supplement 3. In vitro segmentation for M Φ s from dermal tissue.

Figure supplement 4. Time stability of TPE-FLIM parameters for M Φ s isolated from periocular skin in vitro.

Table 1. TPE-FLIM parameters for investigated dermal and epidermal cells.

TPE-FLIM parameters τ_1 , τ_2 , τ_m , a_1/a_2 and TPE-AF intensity of monocyte-derived M1 and M2 M Φ s; dermal M1 and M2 M Φ s isolated from the skin measured in vitro; M1 (CD68) and M2 (CD163) M Φ s measured ex vivo in human skin cryo-sections; M1 and M2 M Φ s observed on the forearm of healthy volunteers in vivo; monocytes; resting and activated human skin mast cells; dendritic cells; fibroblasts and neutrophils in vitro.

		Number of cells	τ_m in ps	τ_1 in ps	τ_2 in ps	a_1/a_2	TPE-AF intensity, photons / mW
in vitro	Monocyte-derived M1-polarised M Φ s	21	479±106	163±50	1,209±161	2.4±0.6	600±100
in vitro	Monocyte-derived M2-polarised M Φ s	27	1,185±170	417±134	2,305±194	2.3±0.5	500±100
in vitro	M1 isolated dermal M Φ s	34	461±175	225±84	1,289±278	4.8±3.4	3,000±500
in vitro	M2 isolated dermal M Φ s	28	1,281±155	807±250	2,352±229	2.2±1.1	800±200
ex vivo	M1 M Φ s (CD68)	8	458±50	190±38	1,504±133	4.1±0.7	3,000±500
ex vivo	M2 M Φ s (CD163)	12	1,369±201	498±129	2,267±155	1.1±0.4	700±300
in vivo	M1 M Φ s	35	477±105	196±40	1,698±172	5.0±2.8	686±165
in vivo	Phagocytosing M1 M Φ s	2	195±44	105±10	1,272±89	14.7±4.5	1,100±150
in vivo	M2 M Φ s	25	1,407±60	442±54	2,458±90	1.2±0.2	360±155
in vitro	PBMC-derived monocytes	15	989±111	491±130	2,025±301	1.8±0.5	700±130
in vitro	Resting mast cells	43	1,248±287	533±266	2,289±317	1.5±0.5	1,300±400
in vitro	Activated mast cells	13	862±268	288±130	1,920±287	2.5±2.0	900±200
in vitro	Dendritic cells	14	1,265±180	434±188	2,578±328	1.6±0.2	538±258
in vitro	Fibroblasts	6	921±81	429±51	1,983±137	0.5±0.1	469±137
in vitro	Neutrophils	21	1,074±109	714±250	1,795±600	1.5±0.5	500±115

showed longer τ_m and significantly lower TPE-AF intensity, typical for M2 M Φ s (**Table 1**, **Figure 2d**, **Figure 3c**). CD68-staining for M1 M Φ s and CD163-staining for M2 M Φ s confirmed that short τ_m cells with high TPE-AF intensity were, indeed, M1 M Φ s (**Figure 3b**) and that cells with longer τ_1 , τ_2 , and τ_m with low TPE-AF intensity were, indeed, M2 M Φ s (**Figure 3d**, **Figure 3—figure supplement 1**, **Table 1**).

CD68-positive dermal M1 M Φ s showed a heterogeneous appearance, ranging from flat and spindle-shaped vessel lining to big intravascular with irregular borders and an irregular nucleus (**Figure 3b**). The TPE-FLIM image of CD163-positive M2 M Φ s show round to elliptically shaped cells with a significantly lower TPE-AF intensity (**Figure 3d**). Of nine cells with a TPE-FLIM M1 M Φ signature, eight cells stained positive for CD68, and all CD68-positive cells had a TPE-FLIM M1 M Φ signature. As for M2 M Φ s, all cells with a TPE-FLIM M2 M Φ signature (12 of 14) were CD163-positive, and all CD163-positive cells had a TPE-FLIM M2 M Φ signature.

TPE-FLIM visualizes human skin M1 and M2 M Φ s in vivo

Next, we used TPE-FLIM to assess the skin of 25 healthy individuals in vivo, and we identified and further characterized 35 and 25 M Φ s with an M1 and M2 TPE-FLIM signature, respectively. In vivo, similar to biopsy sections, M1 and M2 M Φ s were located in the papillary and reticular dermis at >80 μ m depth (**Figure 4**) and showed a density of >100 M Φ s/mm² (**Figure 1c and d**). M1 M Φ s fell into three distinct groups and were either flat and spindle-shaped (**Figure 4a**), slightly dendritic (**Figure 4b**), or large and intervascular (**Figure 4c**). M2 M Φ s, in human skin in vivo, were round and moderately dendritic (**Figure 4d**), and they had a higher TPE-AF intensity in vivo compared to the ECM, as previously reported in vitro (**Malissen et al., 2014; Njoroge et al., 2001**).

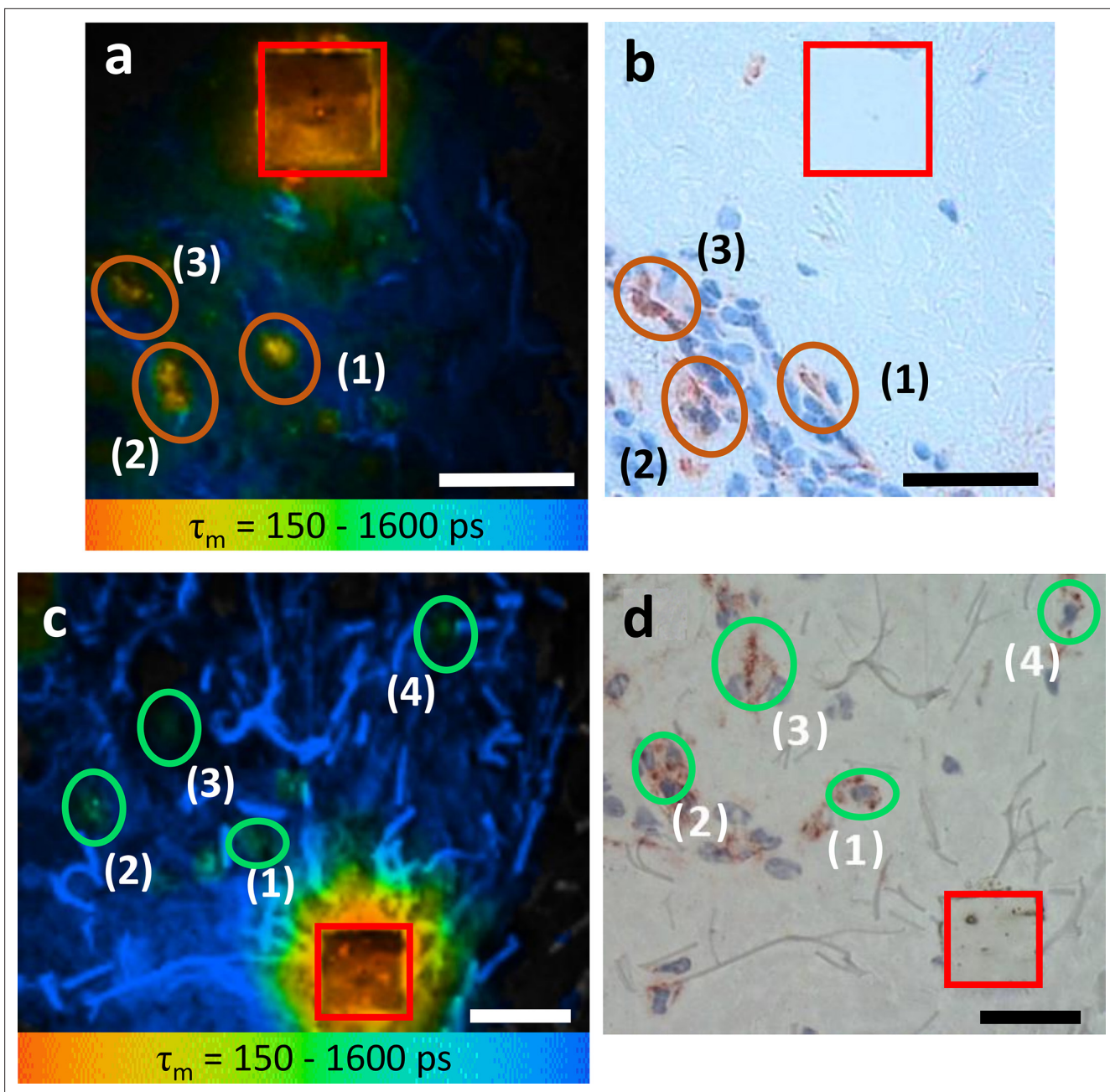


Figure 3. M1 and M2 M Φ s ex vivo verified using TPE-FLIM parameters and immunohistochemistry-based bright field microscopy. Side by side comparison of TPE-FLIM τ_m images (mean fluorescence lifetime τ_m in the 150–1600 ps range), which were measured label-free and then stained with CD68-antibody for M1 M Φ s (a), and CD163-antibody for M2 M Φ s (c) and corresponding bright field microscopic images (b) and (d). The excitation wavelength is 760 nm and laser power is 4 mW (a) and 2 mW (c). The M1 and M2 M Φ s are marked with ellipses in (a, b) and in (c, d), respectively. The laser-burned labels ($28 \times 28 \mu\text{m}^2$) are marked in red. The suspected (a, c) and staining-proved (b, d) M Φ s are marked with number (1, 2, 3, and 4). More M2 M Φ s are observed in (d) compared to (c) due to the staining and visualization of the entire biopsy volume in (d) and limited imaging plane of the two-photon tomograph (1.2–2.0 μm) in (c). Images have been rotated and zoomed to match their orientation and size. Scale bar: 30 μm . TPE-FLIM, two-photon excited fluorescence lifetime imaging.

The online version of this article includes the following figure supplement(s) for figure 3:

Figure supplement 1. Ex vivo segmentation for M Φ s from skin biopsies.

Figure supplement 2. Mast cell-specific staining with tryptase ex vivo – negative control.

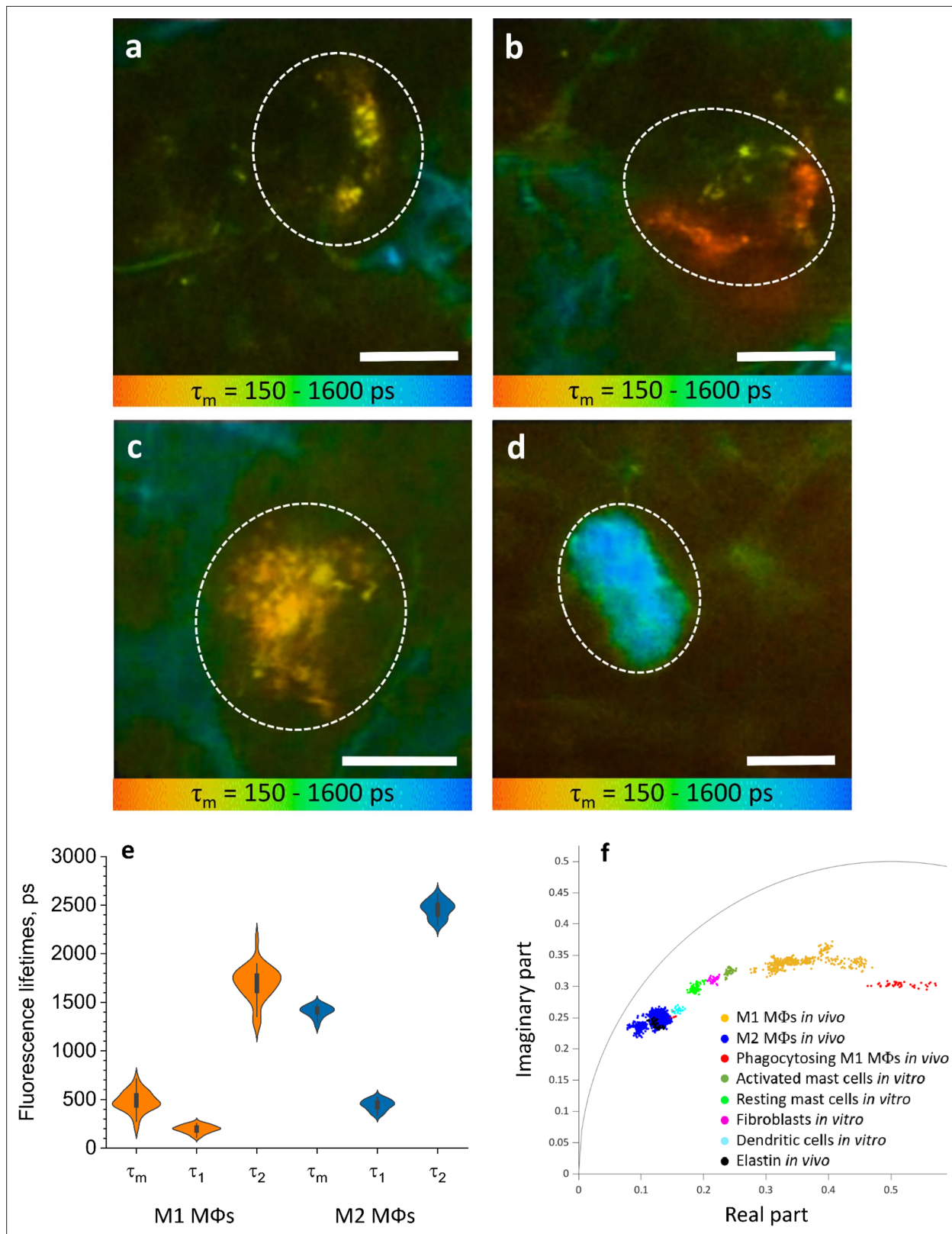


Figure 4. M Φ s are visualized and categorised by TPE-FLIM signatures in vivo. TPE-FLIM in vivo images of potential perivascular flat spindle shaped M1 M Φ (a), of suspected slightly dendritic M1 M Φ in the depth 90 μm (b) large intervascular M1 M Φ with membrane extensions (c) and in vivo dermal cells resembling M2 M Φ were observed with a significantly longer mean fluorescence lifetime τ_m compared to M1 M Φ s and less pronounced TPE-AF intensity (d), showing mean fluorescence lifetime τ_m in color gradient from 150 to 1600 ps. Scale bar: 10 μm . The histogram shows the distribution of

Figure 4 continued on next page

Figure 4 continued

TPE-FLIM parameters for M1 M Φ s ($n=35$, orange) and M2 M Φ s ($n=25$, blue) measured in vivo in human skin (e). The boxplot represents 25–75% of the values. The phasor plot has a threshold at 0.9 of the maximum intensity and shows a summary of 12 M1, 2 phagocytosing M1 M Φ s and 12 M2 M Φ s in vivo (f), where M1 M Φ s are in orange and M2 M Φ s in blue and phagocytosing M1 M Φ s in red, the other dermal components are shown from in vitro measurements. The in vivo images (a–d) were recorded at 760 nm excitation wavelength, 50 mW laser power and 6.8 s acquisition time, in the depth of 80–100 μm on the volar forearm skin area of 25 healthy human subjects. TPE-AF, two-photon excited autofluorescence; TPE-FLIM, two-photon excited fluorescence lifetime imaging.

The online version of this article includes the following figure supplement(s) for figure 4:

Figure supplement 1. In vivo segmentation for M Φ s in human skin.

Figure supplement 2. Time stability of TPE-FLIM parameter for M1 M Φ in vivo.

Figure supplement 3. Time stability of TPE-FLIM parameter for M2 M Φ in vivo.

Figure supplement 4. TPE-FLIM allows for visualization of potentially phagocytosing M1 M Φ s in vivo.

Figure supplement 5. Decision tree model.

Figure supplement 6. ROC curves of decision tree models.

The TPE-FLIM parameters of in vivo M1 M Φ s were in agreement with those of in vitro monocyte-derived and dermal M1 M Φ s and ex vivo M1 M Φ s (Figure 4e, Table 1). M2 M Φ s in vivo have longer τ_m fluorescence lifetimes compared to in vitro and ex vivo experiments. Yet, the τ_1 and τ_2 were in agreement with in vitro PBMC-derived monocytes, and the size and morphological parameters were in line with what is expected in M2 M Φ s. The 2D segmentation in Figure 4—figure supplement 1 shows the distinction of M1 and M2 M Φ s presented in Figure 4a–d, and the phasor plot in Figure 4f shows that M1 and M2 M Φ s could be distinguished from each other and from other dermal cells and ECM.

It should be noted that the TPE-FLIM parameters were stable over the measurements that took up to 30 min for in vivo M1 and M2 M Φ s in the skin (Figure 4—figure supplements 2 and 3). The TPE-FLIM values vary within the standard deviation shown in Table 1.

TPE-FLIM can potentially distinguish resting from phagocytosing human skin M1 M Φ s in vivo

Phagocytosing skin M1 M Φ s are characterized by an increase in cell size (May and Machesky, 2001), enhanced vacuolization (Cheng et al., 2019), a shift of TPE-FLIM parameters toward shorter fluorescence lifetime values (Yakimov et al., 2019), acidification (Li et al., 2017; Teixeira et al., 2018) and thus stimulated ROS production, different from those of resting M1 and M2 M Φ s. A dermal cell matching all these criteria indicating phagocytosis is visualized in vivo using TPE-FLIM and presented in Figure 4—figure supplement 4. This cell is located in the reticular dermis, has an enlarged size ($\approx 25 \mu\text{m}$) and an oval shape, similar to the resting M1 M Φ in Figure 4c, pronounced vacuole structure and short TPE-FLIM lifetime indicative for phagocytosing M1 M Φ . Of 37 dermal M1 M Φ s analyzed in vivo, 2 showed possible phagocytosis activity, and both were located in the reticular dermis below 100 μm of depth.

Classification algorithm to identify M Φ s in the skin

To separate M1 and M2 M Φ s from other dermal cells, we developed a classification algorithm, which used the decision tree (Figure 4—figure supplement 5) and automatically classified M Φ s based on their TPE-FLIM parameters and morphological features. The parameters of the decision tree were improved using hyperparameter optimization. The splitting method in the nodes of the decision tree classifier is chosen to be entropy impurity. To ensure the optimal quality of a split in the node of the decision tree, the following requirements had to be fulfilled: the minimal samples for a split are 2, the maximum depth of the tree is 9, and the samples had equal weight for the model classifying M1 and M2 M Φ s. The independent TPE-FLIM parameters τ_1 , τ_2 , a_1 , and a_2 and the dependent TPE-FLIM variables τ_m , τ_2/τ_1 , a_1/a_2 , $(a_1 - a_2)/(a_1 + a_2)$ have been used for the best classification results, as can be seen in the decision tree model in Figure 4—figure supplement 5. The ground truth was established by classification of in vitro and ex vivo M Φ s with known phenotype resulting in 0.95 ± 0.05 sensitivity and 0.97 ± 0.06 specificity. When M Φ s were classified as one group against other dermal cells, the sensitivity was 0.81 ± 0.03 and the specificity was 0.81 ± 0.03 . Our algorithm also distinguished M1 M Φ s from M2 M Φ s and other cells, with a sensitivity of 0.88 ± 0.04 and a specificity of 0.89 ± 0.03 . For

distinction of M2 M Φ s from M1 M Φ s and other cells, the sensitivity was 0.82 ± 0.03 and the specificity was 0.90 ± 0.03 ; receiver operating characteristic (ROC) is shown in **Figure 4—figure supplement 6**. Additionally, a fivefold cross-validation was additionally executed with these results: (0.87; 0.92; 0.87; 0.89; and 0.94), the mean of k-fold scores using `cross_val_score` method is 0.90 with a score of 1 describing evenly distributed data.

Discussion

This is the first in vivo study to show that human skin M Φ s can be distinguished from other dermal cells and quantified through visualization with label-free, completely noninvasive TPE-FLIM. This risk-free approach also allows for the identification of M Φ phenotypes, that is, M1 and M2 M Φ s, and for the characterization of their functional stage, that is, resting versus phagocytosing M1 M Φ s. Finally, TPE-FLIM can be used to implement sensitive and specific machine learning algorithms for M Φ detection in the skin.

Our initial work with CD-14 positive monocytes isolated from PBMC and then differentiated and polarised toward M1 (IFN- γ) and M2 (IL-4) M Φ s was needed to establish their TPE-FLIM parameters. In fact, it showed that M Φ s are fluorescence-active, and, more importantly, that their TPE-FLIM parameters are among the best differentiators of M1 ($\tau_m=479\pm 106$) and M2 ($\tau_m=1,185\pm 170$) M Φ s. M1 M Φ s are associated with a slightly higher TPE-AF intensity (**Table 1**), which is a prominent indicator for the metabolic stress of the cell on account of a shift in lifetimes by changing amounts of free and bound NAD(P)H (**AlShabany et al., 2016**) and generation of ROS in mitochondria, phagosomal vacuoles, and the cell membrane (**Datta et al., 2015**). Additionally to NAD(P)H, autofluorescence of lipids and other cell compartments was recorded. TPE-AF intensity is a parameter with limitation due to the nonlinear imaging technique. There is no linear correlation between excitation and emission intensity, also it is reduced due to scattering and absorption in the skin. The metabolism of LPS-induced M1 M Φ s is characterized by higher glycolysis, indicating a shift toward shorter fluorescence lifetime (**Li et al., 2020; Orihuela et al., 2016**). The longer fluorescence lifetime τ_2 in M2 M Φ s is best explained by oxidative phosphorylation and the emergence of fluorophores caused by fatty acid oxidation (**Viola et al., 2019**). NAD(P)H fluorescence is ubiquitously present in cells and exhibits the continuum of lifetimes in the 360–3400 ps range. Therefore, changes in TPE-FLIM parameters are likely a reason of the metabolic changes of the M Φ s. Free NAD(P)H has a short lifetime of 360 ps. For bound NAD(P)H, longer lifetimes up to 2–4 ns have been reported (**Alfonso-García et al., 2016**). A higher ratio of bound to free NAD(P)H is associated with M2 M Φ s resulting in longer TPE-FLIM parameters, while a lower ratio of bound to free NAD(P)H is associated with M1 M Φ s resulting in faster TPE-AF decay (**Blacker et al., 2014**). Thus, a strong indicator for the M Φ polarization is the TPE-FLIM parameters of monocytes in between cohorts of M Φ s.

It was observed that the quantity of fluorescence lifetimes in M Φ s is vastly varying between M1 and M2 M Φ s. Regarding the M Φ polarization, the paradigm shifts toward a less strict classification compared to M1 (IFN- γ /LPS-polarized) and M2 (IL-4-polarized). While this categorization is useful in clinical terms, the multitude of parameters leading to the differentiation process leaves M Φ s with wide-ranging properties both in expression of markers and also in appearance and TPE-FLIM parameters (**Murray, 2017**).

M1 (IFN- γ /LPS-polarized) M Φ s rely on the NADH oxidase and production of ROS, which is shown by fluorescent lifetimes of under 250 ps and mitochondrial fission, which can indicate the bright spots, whereas M2 (IL-4-polarized) rely on oxidative phosphorylation and fatty acid oxidation, together with mitochondrial fusion, it can explain the homogeneous appearance of M2 M Φ s (**Ramond et al., 2019; Swindle et al., 2002; Xu et al., 2016**).

Translation of our in vitro findings to M Φ s isolated from human skin confirmed that the latter share the TPE-FLIM signatures of the former, with shorter τ_m in dermal M1 M Φ s and longer τ_m in dermal M2 M Φ s. The classification into M1 and M2 M Φ s in vitro based on their distinct TPE-FLIM parameters was supported by their differences in size, morphology and internal vacuole structure. That the τ_1 lifetime of dermal M2 M Φ s is longer than that of monocyte-derived M2 M Φ s is most likely due to the use of different polarization agents. M Φ colony-stimulating factor (M-CSF) and IFN γ for M1 M Φ s and M Φ colony-stimulating factor (M-CSF) and IL-4 for M2 M Φ s were used in PBMC-derived M Φ s and microenvironment effects, like inflammatory signals, UV exposure (**Kang et al., 1994**), and immune responses (**Theret et al., 2019**) influencing M Φ functions, result in divergent fluorescence lifetimes

(Zhang et al., 2014; Table 1, Figure 2d). The most important outcome of our work with dermal M Φ s was the establishment of their phenotype-specific TPE-FLIM signatures, a prerequisite for our subsequent *in vivo* studies and for comparing skin M Φ s and other dermal cells.

In fact, the use of the TPE-FLIM signatures of M1 and M2 M Φ s clearly allowed to distinguish them from mast cells, dendritic cells, fibroblasts, and neutrophils (Table 1, Figure 4f; Kröger et al., 2020). We controlled this by independent markers. For example, M Φ s exhibited a higher fluorescence intensity compared to other dermal cells. In addition, they were larger than dermal mast cells, and their morphology was clearly different from that of neutrophils and fibroblasts. Vacuoles, a defining feature of M Φ s, were linked to M Φ TPE-FLIM parameters, whereas granules, which identify mast cells, were not. In short, dermal M Φ s, in their TPE-FLIM profiles, do not superimpose with other dermal cells or structures. The only exception, a partial overlap between M2 M Φ s and elastin, is not relevant for the visualization of the former, as they are readily distinguished from the latter based on their morphology.

To confirm that *ex vivo* TPE-FLIM overlap with TPE-FLIM signatures of M1 and M2 M Φ s *in vitro*, we sequentially analyzed cells in skin biopsy cryo sections with TPE-FLIM and conventional immunohistochemistry. Indeed, both approaches identified and distinguished matching M Φ populations, that is, M1 and M2 M Φ s, with strong fluorescence intensity and spindle shape appearance of M1 M Φ s and lower fluorescence intensity and longer fluorescence decay in M2 M Φ s (Figure 3). Interestingly, M2 M Φ s are often found in an area of higher density of unknown dermal cells, presumably fibroblasts, compared to M1 M Φ s. It is suspected that M2 M Φ s in conjunction with collagen-synthesizing fibroblasts are acting toward and aiding in dermal repair and regeneration. However, this approach also revealed some challenges that come with M Φ visualization by TPE-FLIM. For example, it was more difficult to visualize M2 M Φ s than M1 M Φ s in biopsies due to the high fluorescence intensity of elastin in dried tissue and other ECM components and a decreased signal-to-noise ratio. In Figure 3d, more CD163 positive M2 M Φ s are visible compared to the corresponding TPE-FLIM image in Figure 3c, which is due to previously mentioned challenges and the limited imaging plane of the two-photon tomograph (1.2–2.0 μ m) compared to a significantly thicker biopsy section (10 μ m), which was stained in an entire depth and visualized by bright field microscopy. Importantly, immunohistochemistry confirmed our M Φ phenotype-specific TPE-FLIM signatures, and, in addition, confirmed that they distinguish M Φ s from other dermal cells. Skin mast cells, for example, stained for tryptase, showed a distinct TPE-FLIM signature, confirming our recently reported findings on dermal mast cells *in vivo* (Kröger et al., 2020), and distinguished them from M1 and M2 M Φ s (Figure 3—figure supplement 2).

When we turned to the visualization of skin M Φ s *in vivo*, we had first to develop a search strategy. Important considerations included the preferred localization of M Φ s in the papillary and reticular dermis, the orientation of the focal plane parallel to the skin surface, and the need for maximal cellular cross-section visualization, which requires a high-resolution adjustment in depth to reconstruct an entire cell structure. The application of this search algorithm successfully visualized M1 and M2 M Φ s in human skin *in vivo*. The *in vivo* TPE-FLIM parameters of M1 M Φ s were in agreement with those observed *in vitro* and *ex vivo*. M2 M Φ s *in vivo* were characterized by longer mean fluorescence lifetime τ_m compared to *in vitro* and *ex vivo* (Table 1), which can be explained by the influence of environment (Koo and Garg, 2019; Njoroge et al., 2001). M Φ s measured *in vivo* differ from cells measured *in vitro* by their simplified microenvironment (Mosser and Edwards, 2008) with missing growth factors and cytokines (Melton et al., 2015) and an elevated level of nutrients, which leads to different polarization of M Φ s and different contributions of fluorescence lifetimes. Membrane extensions were harder to detect *in vivo* due to the obscuring effect of the surrounding ECM. We also observed that TPE-FLIM parameters in the same M Φ s can vary depending on their cellular substructures, for example, the nucleus, vacuoles, cytoplasm, or membrane (Figure 4a–d). The phasor plot shows the relative position of the categories of M Φ s and other cells. Furthermore, it shows the contributions of long and short fluorescence lifetimes, their discrepancies (Table 1) being due to the computational method and the harmonics at the repetition frequency of 80 MHz. Further investigations are needed to clarify how the location, morphology, and function of M1 and M2 M Φ s influence their TPE-FLIM parameters and TPE-AF intensity *in vivo*. Such studies should also address the reasons for the differences in TPE-FLIM parameters between M1 and M2 M Φ s, which may include differences in their metabolic pathways. M1 M Φ s, for example, rely on NADH oxidase and production of ROS, which is linked to short fluorescence lifetimes below 250 ps and mitochondrial fission. M2 M Φ s, on

the other hand, rely on oxidative phosphorylation and fatty acid oxidation, together with mitochondrial fusion (Ramond et al., 2019; Swindle et al., 2002; Xu et al., 2016).

The ability to visualize M1 and M2 M Φ s by TPE-FLIM *in vivo* also makes it possible to explore how and why M Φ s' morphology, location, and functions are linked. When activated, the cytoskeletal structure and cellular appearance of M Φ s change, and this may also affect their TPE-FLIM parameters. M1 M Φ s are elongated, with a dense actin network along the cortex. M2 M Φ s are more spherical with more randomly distributed actin (Porcheray et al., 2005; Vogel et al., 2014; Zhang et al., 2014; Figure 4b and d). Actin reorganization in M1 and M2 M Φ polarization and activation lead to bigger filament bundles of the actin cytoskeleton, which reduces cell plasticity (Colin-York et al., 2019; Pergola et al., 2017). As reported by Vogel et al., 2014, M Φ migration in the skin depends on their polarization. M1 M Φ s, due to changes in actin cytoskeleton, migrate less far than M2 M Φ s. Our TPE-FLIM findings confirm this, as we detected M1 M Φ s via their high fluorescence and short auto-fluorescence lifetimes primarily in close proximity to blood capillaries. The irregular appearance of M1 M Φ detected by TPE-FLIM is likely a consequence of polarization-specific changes of the cellular cytoskeleton (McWhorter et al., 2013). The only morphological feature observed in both, M1 and M2 populations of M Φ s, is that they are moderately dendritic, possibly because such M Φ s are in the process of polarization, prior to cytoskeletal changes (Sica and Mantovani, 2012), or because polarization in M Φ s is reversible polarizing (Sica and Mantovani, 2012; Yuan et al., 2017). Future studies should characterize the influence of cytoskeletal changes on TPE-FLIM parameters in detail and use TPE-FLIM to assess the impact of age, gender, and disease on the ratio, localization, and function of M1 and M2 M Φ s in the skin (Fukui et al., 2018).

Time stability measurements were performed *in vitro* on M1 and M2 M Φ s isolated from periocular skin within 1 hr (Figure 2—figure supplement 4) and *in vivo* on M1 M Φ within 30 min (Figure 4—figure supplements 2 and 3).

TPE-FLIM parameters were stable and varied within the standard deviation range shown in Table 1. It was possible to visualize single cells over this long-term time period *in vitro* (Figure 2—figure supplement 4) and *in vivo* (Figure 4—figure supplements 2 and 3), yet no unprompted change in fluorescence lifetime was observed, given the laser power was not high enough to induce photo-products or photobleaching of the fluorophores. The NAD(P)H-related TPE-FLIM parameter showed no change over the course of the measurement nor did the fluorescence intensity. The limitation of long-term *in vitro* measurements is that the cells cannot be heated and will eventually cool down to room temperature. The limitation of long-term *in vivo* measurements is inherent to the individual. It is technically possible to investigate one subject over the course of multiple hours, but it is almost impossible to find the same cell again in another measurement.

Another limitation of this study is the simplified separation between M1 and M2 M Φ s without taking into consideration the mixed M Φ phenotype. As mentioned in the introduction, mixed phenotype of M Φ s is primarily observed in diseases like melanoma, systemic sclerosis, Lupus, and in recovery from LPS tolerance. Thus, we do not expect a significant amount of mixed phenotype M Φ s in healthy and asymptomatic skin. However, the M Φ s misidentified by the decision tree (Figure 2—figure supplement 3 and Figure 4—figure supplement 1) could potentially be M Φ s of a mixed phenotype, which should be proved in additional experiment.

During phagocytosis, the generation of ROS by NAD(P)H oxidase leads to the highest degree of metabolic stress observed in M1 M Φ s besides apoptosis (Dupré-Crochet et al., 2013; Shirshin et al., 2019), and ROS localization in vacuoles in phagocytosing M1 M Φ s as a bactericidal mechanism (Dupré-Crochet et al., 2013; Myers et al., 2003). This is why phagocytosing M1 M Φ s change their TPE-FLIM lifetimes toward shorter values and their vacuoles become visible as localized bright spots, which makes their *in vivo* detection possible (Figure 4—figure supplement 4, Table 1; Cannon and Swanson, 1992). The results shown here for possible phagocytosis are supported by the appearance (large size) and shortened fluorescence lifetime values for erythrophagocytosing cells, presented by our group (Yakimov et al., 2019), resembling the cell shown in this study. The microenvironment in inflamed skin is known to be acidic with a pH<7.35 (Haka et al., 2009). Acidification is also known in phagocytosing M Φ s (Teixeira et al., 2018). Together with the fact that fluorescence lifetime of fluorophores is shifted toward shorter values (Li et al., 2017) and cells especially M Φ s produce ROS under phagocytosis and acidic conditions (Slauch, 2011), we have very compelling indications for the visualization of phagocytosing M1 M Φ s. The influence of different phagocytosed materials in M Φ s

should be investigated in the future. TPE-FLIM potentially allows for the detection of possible phagocytosing M1 M Φ s and is used as a confounder in the classification but cannot detect what is phagocytized. No internal structure was visible in TPE-FLIM images. The precision of measurements of cells and structures with short fluorescence lifetimes, such as phagocytosing M Φ s, could be improved by reducing the value of the instrument response function (IRF), which is <100 ps in our measurements.

The construction of the feature vector and the resulting hyperparameter optimized decision tree model (**Figure 4—figure supplement 5**) yielded proficient results for the automatized classification of M1 and M2 M Φ s, demonstrating that M1 and M2 M Φ s can be separated from each other and other cells in the skin with high accuracy, that is, sensitivity and specificity, without need of additional staining using a supervised machine learning approach. The decision tree model uses only the independent TPE-FLIM parameters τ_1 , τ_2 , a_1 , and a_2 and the dependent TPE-FLIM variables τ_m , τ_2/τ_1 , a_1/a_2 , $(a_1 - a_2)/(a_1 + a_2)$. This indicates that macrophages could be distinguishable completely from other cells without the use of morphologic parameters, thus reducing the degree of freedom and saving calculation and annotation time by software and physicians. The high accuracy for M1 macrophages is owed to the fact that M1 M Φ s have the shortest τ_1 and τ_2 fluorescence lifetimes, the highest ratio of a_1/a_2 and the highest fluorescence intensity of the cells in the model. M2 M Φ s can be misclassified in rare cases with resting mast cells and in vitro dendritic cells. Concluding from these results that the classification is only dependent on TPE-FLIM parameters and not on the morphology of dermal cells.

Ideally the data sets consist of the same amount of entries for every three classes (M1 M Φ s, M2 M Φ s, and other cells). In the experimental reality, those three classes are not evenly distributed and could lead to overemphasize of certain classes in the classifier model. It is shown here by the methods above that the data set is useable for the decision tree classifier. Overfitting of the relatively small data set is avoided with the parameters for the decision tree model, first by randomly splitting the data set into training and test set 10,000 times resulting in a small standard deviation and with the use of k-fold cross-validation resulting in a mean of the cross-validation score of 0.90, which equates to 90% accuracy. A cross-validation score of 1 describes perfectly even distributed data in all folds. The robustness and accuracy of this approach can be improved further, by the introduction of a depth-adjusted cell size and refined cell shape parameters and by increasing the number of in vivo M Φ s integrated into the algorithm and training data set.

Materials and methods

Two-photon excited fluorescence lifetime imaging

For imaging of human M Φ s, a two-photon tomograph (Dermainspect, JenLab GmbH, Jena, Germany), equipped with a tunable femtosecond Ti:sapphire laser (Mai Tai XF, Spectra Physics, USA, 710–920 nm, 100 fs pulses at a repetition rate of 80 MHz), was used at 3–5 mW for measurements of cells in vitro and skin biopsy sections ex vivo, as well as human dermis in vivo at 40–50 mW. The excitation wavelength was set to 760 nm, and a 410–680 nm band pass filter was used to detect two-photon excited autofluorescence (TPE-AF), whereas a 375–385 nm band pass filter was used to detect the second harmonic generation signals. The axial and lateral resolution was approximately 1.2–2.0 and 0.5 μ m, respectively (**Breunig et al., 2013**). The screening depth covers the entire papillary dermis and part of reticular dermis (**Darvin et al., 2014; König, 2008; Kröger et al., 2020**).

Fluorescence decay of a specimen was recorded and analyzed in the SPCImage 8.0 software (Becker&Hickl, Berlin, Germany). TPE-FLIM data were fitted with a bi-exponential decay function. The TPE-AF intensity threshold was chosen depending on the signal-to-noise ratio, minimizing noise in the region of interest. The shift of the signal in relation to the instrument response function (IRF) was compensated. The typical IRF value was <100 ps. The TPE-AF decay curves were averaged over the central pixel of the region of interest and the 48 closest square neighbouring pixels (binning=3), resulting in a number of detected photons for each fluorescence decay curve larger than 5000. The TPE-AF decay parameters, decay lifetimes (τ_1 and τ_2) and amplitudes (a_1 and a_2), were used for the evaluation of the fluorescence lifetime distributions and 2D segmentation (**Shirshin et al., 2017**). The analyzed parameters were the mean lifetime, defined as $\tau_m = (a_1\tau_1 + a_2\tau_2)/(a_1 + a_2)$ and the ratios τ_2/τ_1 , a_1/a_2 and $(a_1 - a_2)/(a_1 + a_2)$, which were used for 2D segmentation analysis. The TPE-FLIM data were also analyzed and represented as phasor plots, that are based on the transformation of the fluorescence decay data in the frequency domain, whereas the decay is described as amplitude and phase values of

the first Fourier component (*Digman et al., 2008*). The phasor plots' x-axis is described by the cosine of the phase value multiplied by the amplitude, the y-axis represents the sine of the phase value multiplied by the amplitude (*Lakner et al., 2017; Shirshin et al., 2019*). The position of the mean lifetime is on the secant from τ_1 and τ_2 , the distance to the circle is given by the proportion of a_1 and a_2 . The TPE-FLIM data were normalized to the maximum intensity and the threshold of 70% was set when analysing the phasor plots. The comparison of the bi-exponential fitting and phasor analysis in separation between cells subpopulations when treating the FLIM data was analyzed in *Shirshin et al., 2022*—in this work, we used both approaches to separate the M1 and M2 macrophages.

FLIM data processing

The fluorescence decay curves were fitted with the bi-exponential decay model. Justification of the choice of the model and its comparison to the three exponential fitting is presented in the SI (Section FLIM data analysis). The absence of correlations between the fluorescence intensity and fluorescence decay parameters, as well as for fitting quality (assessed as χ^2) and fluorescence decay parameters was additionally verified as described in the SI.

Ethical considerations and study conduct

Volunteers for intravital imaging provided their written informed consent before participation. Skin samples taken from periocular skin surgery for M Φ preparation and all human skin investigated in this study were used after written informed consent was obtained. Positive votes for the experiments have been obtained from the ethics committee of the Charité – Universitätsmedizin Berlin (EA1/078/18, EA4/193/18, and EA1/141/12), which were conducted according to the Declaration of Helsinki (59th WMA General Assembly, Seoul, October 2008).

Study subjects

Twenty-five healthy volunteers (12 males and 13 females, 24–65 years old, skin type I–III according to *Fitzpatrick, 1988* classification) with asymptomatic volar forearm skin without preexisting health conditions were randomly selected for noninvasive in vivo measurements in the papillary dermis using TPE-FLIM. Visually impairing hair was removed with a scissor prior to measurements. The oil immersion objective of the microscope was connected to the skin via a 150 μm thick, 18 mm diameter cover glass (VWR, Darmstadt, Germany) with a ≈ 10 μl distilled water droplet between cover glass and skin. About 6–12 in vivo tomograms (different skin areas) were measured per subject, the investigated volume is from ≈ 70 μm depth in the papillary dermis to ≈ 130 μm depth in the reticular dermis with an image size of 150×150 μm^2 . This adds up to $(60 \times 150 \times 150)$ μm^3 times 6–12 images, with a total volume of 0.008–0.016 mm^3 of papillary and reticular dermis seen per subject, the average time spent was ≈ 30 min per subject and the acquisition time was 6.8 s per image. The volunteers were screened between October 2018 and November 2020.

Investigation of human dermal M Φ s in vitro

Human dermal M Φ s were prepared from periocular tissue (*Botting et al., 2017*). Human periocular skin was digested in 2.4 U/ml dispase type II (Roche, Basel, Switzerland) at 4°C for 12 hr. The dermis was minced with scissors after removal of the epidermis and further digested in PBS containing Ca^{2+} and Mg^{2+} (Gibco, Carlsbad, CA) supplemented with 1% Pen/Strep, 5% FCS, 5 mM MgSO_4 , 10 $\mu\text{g}/\text{ml}$ DNaseI (Roche), 2.5 $\mu\text{g}/\text{ml}$ amphotericin (Biochrom, Berlin, Germany), 1.5 mg/ml collagenase type II (Worthington Biochemical Corp, Lakewood, NJ), and 0.75 mg/ml H-3506 hyaluronidase (Sigma-Aldrich, St. Louis, MO) at 37°C in a water bath with agitation for 60 min. The cell suspension was filtered using 300 and 40 μm stainless steel sieves (Retsch, Haan, Germany). Centrifugation at $300 \times g$ for 15 min at 4°C was applied next. The digestion cycle was repeated once. M Φ s were isolated by Pan Monocyte Isolation Kit (Miltenyi, Bergisch Gladbach, Germany) after washing in phosphate-buffered saline (PBS) w/o Ca^{2+} and Mg^{2+} (Gibco), and kept in basal Iscove's medium supplemented with 1% Pen/Strep, 10% FCS, 1% non-essential amino acids, 226 μM α -monothioglycerol (all Gibco). For long-term cultures, after 24 hr recombinant human IL-4 (20 ng/ml) and hSCF (100 ng/ml) (both Peprotech, Rocky Hill, NJ) were added. Purity of M Φ cultures was routinely checked to be $>85\%$ (*Nielsen et al., 2020*). For imaging, cells were used after 3 days in medium, washed two times with PBS before

seeding on 18 mm diameter microscope cover glass (VWR) for imaging in PBS containing Ca^{2+} (Gibco) at room temperature.

Investigation of peripheral blood monocytes in vitro

Peripheral blood monocytes were isolated from human blood using 15 ml Ficoll-Paque (VWR) centrifugation gradient. Centrifugation was performed at $1000\times g$ for 1 min, with added 9 ml heparin and filled to 50 ml with PBS. Centrifugation was then repeated at $1000\times g$ for 10 min, discarding the upper plasma layer and collecting the PBMC layer. The cells were washed two times with PBS and centrifuged at $350\times g$ for 10 min. The supernatant was discarded and cultured in 5 ml basal Iscove's medium supplemented with 1% Pen/Strep, 10% FCS (Biochrom, Berlin, Germany) and subsequently incubated at 37°C and 5% CO_2 for 2 hr before seeded and imaged on an 18 mm diameter microscope cover glass (VWR) in PBS containing Ca^{2+} (Gibco) at room temperature.

Investigation of M Φ s differentiated from peripheral blood monocytes in vitro

M Φ s were differentiated from peripheral blood monocytes and polarised into M1 (IFN γ)-like state with M Φ colony-stimulating factor (M-CSF) and IFN γ and M2 (IL-4)-like state with M Φ colony-stimulating factor (M-CSF) and IL-4. For further stimulation, cells were incubated with LPS at 37°C for 24 hr prior to imaging. Due to a simplified environment with specific differentiation agents, the differentiation of monocytes was partially incomplete. Exemplary monocyte-derived M Φ s appearing as M1 or M2 M Φ s were measured and analyzed by TPT/FLIM. The requirement for M1 M Φ s was a granular appearance and for M2 M Φ s a dendritic appearance.

Investigation of dendritic cells in vitro

CD14 positive PBMCs were used to differentiate dendritic cells by washing in PBS and centrifuging at $350\times g$ for 10 min two times. About 5 ml RPMI medium, supplemented with 1% Pen/Strep and 1% FCS (Biochrom), was added. Tryptan Blue (Sigma-Aldrich) was used for counting the cells in a hemocytometer, seeded at 2.0×10^6 cells/ml and incubated for 2 hr at 37°C under 5% CO_2 . Non-attached cells and the supernatant were discarded. Adding 500 μl basal Iscove's medium to the cells supplemented with 1% Pen/Strep, 1% glutamine, 5% HSA (all Gibco), 100 ng/ml IL-4, 100 ng/ml GM-CSF (both Peprotech) with medium change every second day for 6 days at 37°C . For TPE-FLIM imaging, the cells were seeded on 18 mm diameter microscope cover glass (VWR) in PBS containing Ca^{2+} at room temperature.

Preparation and cryo-sectioning of human skin for combined TPE-FLIM and histomorphometric analysis

Thirteen human skin biopsy cryo-sections were prepared and measured using the TPE-FLIM method to acquire TPE-FLIM parameters of suspected M1 and M2 M Φ s. The skin biopsies were obtained from abdominal reduction surgery of four female patients (31, 33, 40, and 44 y. o., skin type II according to Fitzpatrick classification; *Fitzpatrick, 1988*). Punch biopsies of 6 mm diameter were obtained, frozen, and stored at -80°C before cryo-sectioning. Vertical histological cryo-sections of 10 μm thickness were prepared on a cryostat (Microm Cryo-Star HM 560, MICROM International GmbH, Walldorf, Germany) after embedding in a cryo-medium (Tissue Freezing Medium, Leica Biosystems Richmond Inc, Richmond, IL) and placed on 18 mm diameter microscope cover glasses (VWR). The anatomical condition of the biopsies was continuously examined using a transmission microscope (Olympus IX 50, Olympus K.K., Shinjuku, Tokyo, Japan).

Using TPE-FLIM, cryo-sections were searched for cells with M Φ -specific TPE-FLIM parameters and the corresponding TPE-FLIM images of suspected M Φ s were recorded. To prove the measured cells are M Φ s, the skin biopsies were labeled by irradiating a squared area of $28\times 28\ \mu\text{m}^2$ located near the suspected M Φ s with a Ti:sapphire laser (Mai Tai XF, Spectra Physics, USA, 100 fs pulses at a repetition rate of 80 MHz) at a maximal power of 50 mW at 760 nm for 3 s. All incubations were performed at room temperature unless otherwise stated. In brief, sections were fixed for 10 min in cold acetone (-20°C) and rinsed in TBS (Agilent Technologies, Santa Clara, CA). For staining of M Φ s, the M Φ -specific anti-CD68 (clone ab955) (Abcam, Cambridge, UK), Recombinant Anti-CD163 antibody [EPR14643-36] (clone ab189915) (Abcam) were used to account for M1

and M2 $\text{M}\Phi$ phenotypes, respectively. Slides were rinsed three times with TBS, and endogenous peroxidase was blocked with 3% H_2O_2 in TBS for 5 min followed by incubation with anti-mouse EnVision+ labeled polymer (Agilent Technologies) for 30 min. Slides were rinsed in TBS as before and incubated with AEC substrate-chromogen (Agilent Technologies) for 10 min. Nuclei were counterstained with Mayer's hemalum solution (Merck, Darmstadt, Germany). Stained $\text{M}\Phi$ s have a brown-red color, which enables to visually distinguish them from other cells and the ECM. After the staining procedure, target $\text{M}\Phi$ s and squared labels of the skin sections were identified by light microscopy and overlaid with TPE-FLIM images matching an appropriate magnification and image orientations.

Specifically, CD68-stained M1 $\text{M}\Phi$ s were counted in the papillary dermis region in each biopsy, and an average of 209 ± 25 cells/ mm^2 for the papillary dermis and an average of 140 ± 76 cells/ mm^2 for the reticular dermis for a 10 μm deep cryo-section was observed (**Figure 1c**). The density of the CD163 stained M2 $\text{M}\Phi$ s was an average of 242 ± 126 cells/ mm^2 for the papillary dermis and an average of 107 ± 60 cells/ mm^2 for the reticular dermis for a 10 μm deep cryo-section (**Figure 1d**).

The $\text{M}\Phi$ s search algorithm we then used was similar to that recently presented by our group for the identification of resting and activated mast cells in the papillary dermis (**Kröger et al., 2020**) and included the following steps: first, the papillary dermis (≈ 60 – 100 μm depth for volar forearm) was explored for fluorescent spots of 10–15 μm in size with irregular shape and a membrane extension having bright spots of about 1–3 μm . The TPE-FLIM parameters of the suspected bright areas were measured and matched those of M1 and M2 $\text{M}\Phi$ s obtained in vitro and ex vivo.

To prove that the TPE-FLIM parameters of other dermal cells, which have detectable TPE-AF intensity, namely, mast cells and dendritic cells do not match or superimpose with TPE-FLIM parameters of $\text{M}\Phi$ s, negative control measurements were performed. The procedure was similar as described for the verification of $\text{M}\Phi$ s in skin biopsies using specific immunofluorescence, but six human skin cryo-sections were stained for the presence of mast cells and two for dendritic cells.

Staining of mast cells was done by blocking with serum-free protein followed by incubation for 1 hr with anti-tryptase antibody (clone AA1) diluted 1:1000 in antibody diluent (all Agilent Technologies). For staining of dendritic cells, anti-CD11c antibody (clone B-Ly6) (BD Biosciences, Franklin Lakes, NJ) was used after fixing the cryo-section for 10 min in cold acetone (-20°C) and rinsing with TBS.

Statistical analysis and classification algorithm

Matlab R2016a (MathWorks, Natick, MA) was applied for descriptive statistics of all TPE-FLIM data. All results are indicated as mean \pm standard deviation. Differences between distributions were compared using the nonparametric Kolmogorov-Smirnov test with a significance level of $\alpha=0.05$. The decision tree classifier was modelled using Scikit-learn 0.22 in a Python 3.7 environment (Python Software Foundation, Wilmington, DE). A randomised training set, consisting of 50% of the complete data set, was used for training and validating the test set 10,000 times. The true positive and true negative rates were calculated from the confusion matrix and describe the quality of the classification and indicate type I and type II errors. For the decision tree (**Breiman et al., 1984**), the TPE-FLIM parameters τ_1 , τ_2 , τ_m , τ_1/τ_2 , a_1 , a_2 , a_1/a_2 , $(a_1-a_2)/(a_1+a_2)$, TPE-AF intensity, cell shape, and decay curve were used for each cell measured in vitro, ex vivo, and in vivo and hyperparametrically optimized (**Yang and Shami, 2020**). The feature vector was constructed as follows: 8 (TPE-FLIM parameters obtained after bi-exponential approximation of the decay curve), in total, 8 values. The $\text{M}\Phi$ size was not included in the feature vector for the classification model, as $\text{M}\Phi$ s in vivo could have slightly different dimensions from those measured in vitro (in cell cultures) and ex vivo (in biopsies), caused by obscuring effects of surrounding dermal tissue. Here, 1 represents circular and 0 noncircular shape. The lifetimes calculated from the bi-exponential decay model were averaged over the whole cell, and the fluorescence intensity was normalized by optical power and averaged the pixel of interest and the 48 neighbouring square pixel.

In total, 110 $\text{M}\Phi$ s in vitro, 20 $\text{M}\Phi$ s ex vivo, 70 $\text{M}\Phi$ s in vivo (for M1/M2 ratio see **Table 1**), 59 mast cells in vitro, 17 mast cells ex vivo, 82 mast cells in vivo, 14 dendritic cells in vitro, 6 fibroblasts in vitro, and 21 neutrophils in vitro were used as input for the model (399 cells in total). Given data vectors from $x_i \in R^n$, $i=1, \dots, l$ and a label vector $y_i \in R^l$, where a decision tree recursively separates the data into two classes with the mode m represented as Q . For each node a split $\theta = (j, t_m)$ decided with the feature j and the threshold t_m . The node split the data into subsets $Q_{\text{left}}(\theta)$ and $Q_{\text{right}}(\theta)$.

$$Q_{left}(\theta) = (x, y) | x_j \leq t_m$$

$$Q_{right}(\theta) = Q \setminus Q_{left}(\theta)$$

The impurity was calculated by the impurity function $H()$ at the mode m

$$G(Q, \theta) = \frac{n_{left}}{N_m} H(Q_{left}(\theta)) + \frac{n_{right}}{N_m} H(Q_{right}(\theta))$$

With the parameters for minimized impurities, the subsets were recourse until $N_m=1$.

The return values of the classification were 0 for M1 MΦs, 1 for M2 MΦs, and 2 for other dermal cells, 0 for MΦs and 1 for other dermal cells for node m in the region R_m and N_m observation, the proportion of class k observations in node m is $p_{mk} = 1/N_m \sum_{x_i \in R_m} I(y_i = k)$.

ROC curves served as a tool to determine the diagnostic abilities of the method, where the true positive rate was plotted against the false positive rate of the respective outcomes for both the categorization of MΦs against other dermal cells and M1 MΦs and M2 MΦs against other dermal cells.

Acknowledgements

The authors thank Evelin Hagen, Niklas Mahnke, and Loris Busch from Charité – Universitätsmedizin Berlin for their excellent technical support. The authors thank David Satzinger for the schematic illustration of MΦs. Foundation for Skin Physiology of the Donor Association for German Science and Humanities (Marius Kröger, Johannes Schleusener, Martina C Meinke, Jürgen Lademann, Maxim E Darwin) Russian Science Foundation No. 19-75-10077 "Photonic and Quantum technologies. Digital medicine" (Evgeny A Shirshin).

Additional information

Funding

Funder	Grant reference number	Author
Foundation for Skin Physiology		Marius Kröger
Russian Science Foundation	19-75-10077	Evgeny A Shirshin

The funders had no role in study design, data collection and interpretation, or the decision to submit the work for publication.

Author contributions

Marius Kröger, Data curation, Software, Formal analysis, Investigation, Writing – original draft; Jörg Scheffel, Resources, Data curation, Investigation, Methodology, Writing - review and editing; Evgeny A Shirshin, Formal analysis, Validation, Methodology, Writing - review and editing; Johannes Schleusener, Formal analysis, Validation, Investigation, Methodology, Writing - review and editing; Martina C Meinke, Resources, Supervision, Funding acquisition, Project administration, Writing - review and editing; Jürgen Lademann, Conceptualization, Resources, Supervision, Funding acquisition, Methodology, Writing - review and editing; Marcus Maurer, Conceptualization, Data curation, Supervision, Funding acquisition, Methodology, Writing – original draft; Maxim E Darwin, Conceptualization, Data curation, Formal analysis, Supervision, Validation, Methodology, Writing – original draft, Project administration

Author ORCIDs

Marius Kröger  <http://orcid.org/0000-0002-0148-4225>

Maxim E Darwin  <http://orcid.org/0000-0003-1075-1994>

Ethics

Human subjects: Positive votes for the experiments have been obtained from the ethics committee of the Charité; - Universitätsmedizin Berlin (EA1/078/18, EA4/193/18, EA1/141/12), which were

conducted according to the Declaration of Helsinki (59th WMA General Assembly, Seoul, October 2008).

Decision letter and Author response

Decision letter <https://doi.org/10.7554/eLife.72819.sa1>

Author response <https://doi.org/10.7554/eLife.72819.sa2>

Additional files

Supplementary files

- Transparent reporting form

Data availability

The data have been deposited in Dryad.

The following dataset was generated:

Author(s)	Year	Dataset title	Dataset URL	Database and Identifier
Kröger M, Darvin M	2021	Macrophage FLIM raw data	https://dx.doi.org/10.5061/dryad.8gtht76q2	Dryad Digital Repository, 10.5061/dryad.8gtht76q2

References

- Alfonso-García A**, Smith TD, Datta R, Luu TU, Gratton E, Potma EO, Liu WF. 2016. Label-free identification of macrophage phenotype by fluorescence lifetime imaging microscopy. *Journal of Biomedical Optics* **21**:46005. DOI: <https://doi.org/10.1117/1.JBO.21.4.046005>, PMID: 27086689
- AlShabany AJ**, Moody AJ, Foey AD, Billington RA. 2016. Intracellular NAD⁺ levels are associated with LPS-induced TNF- α release in pro-inflammatory macrophages. *Bioscience Reports* **36**:e00301. DOI: <https://doi.org/10.1042/BSR20150247>, PMID: 26764408
- Arango Duque G**, Descoteaux A. 2014. Macrophage cytokines: involvement in immunity and infectious diseases. *Frontiers in Immunology* **5**:1–12. DOI: <https://doi.org/10.3389/fimmu.2014.00491>, PMID: 25339958
- Bardi GT**, Smith MA, Hood JL. 2018. Melanoma exosomes promote mixed M1 and M2 macrophage polarization. *Cytokine* **105**:63–72. DOI: <https://doi.org/10.1016/j.cyto.2018.02.002>, PMID: 29459345
- Benoit M**, Desnues B, Mege JL. 2008. Macrophage polarization in bacterial infections. *Journal of Immunology* **181**:3733–3739. DOI: <https://doi.org/10.4049/jimmunol.181.6.3733>, PMID: 18768823
- Blacker TS**, Mann ZF, Gale JE, Ziegler M, Bain AJ, Szabadkai G, Duchon MR. 2014. Separating NADH and NADPH fluorescence in live cells and tissues using FLIM. *Nature Communications* **5**:3936. DOI: <https://doi.org/10.1038/ncomms4936>, PMID: 24874098
- Botting RA**, Bertram KM, Baharlou H, Sandgren KJ, Fletcher J, Rhodes JW, Rana H, Plasto TM, Wang XM, Lim JJK, Barnouti L, Kohout MP, Papadopoulos T, Merten S, Olbourne N, Cunningham AL, Haniffa M, Harman AN. 2017. Phenotypic and functional consequences of different isolation protocols on skin mononuclear phagocytes. *Journal of Leukocyte Biology* **101**:1393–1403. DOI: <https://doi.org/10.1189/jlb.4A1116-496R>, PMID: 28270408
- Breiman L**, Friedman JH, Olshen RA, Stone CJ. 1984. Classification and Regression Trees, The Wadsworth Statistics/Probability Series. Monterey, CA: Wadsworth & Brooks/Cole Advanced Books & Software.
- Breunig HG**, Weinigel M, Bückle R, Kellner-Höfer M, Lademann J, Darvin ME, Sterry W, König K. 2013. Clinical coherent anti-stokes raman scattering and multiphoton tomography of human skin with a femtosecond laser and photonic crystal fiber. *Laser Physics Letters* **10**:025604. DOI: <https://doi.org/10.1088/1612-2011/10/2/025604>
- Cannon GJ**, Swanson JA. 1992. The macrophage capacity for phagocytosis. *Journal of Cell Science* **101** (Pt 4):907–913. DOI: <https://doi.org/10.1242/jcs.101.4.907>, PMID: 1527185
- Cheng J**, Zhang Q, Fan S, Zhang A, Liu B, Hong Y, Guo J, Cui D, Song J. 2019. The vacuolization of macrophages induced by large amounts of inorganic nanoparticle uptake to enhance the immune response. *Nanoscale* **11**:22849–22859. DOI: <https://doi.org/10.1039/c9nr08261a>, PMID: 31755508
- Chong BF**, Tseng L-C, Hosler GA, Teske NM, Zhang S, Karp DR, Olsen NJ, Mohan C. 2015. A subset of CD163⁺ macrophages displays mixed polarizations in discoid lupus skin. *Arthritis Research & Therapy* **17**:324. DOI: <https://doi.org/10.1186/s13075-015-0839-3>, PMID: 26568320
- Colin-York H**, Li D, Korobchevskaya K, Chang VT, Betzig E, Eggeling C, Fritzsche M. 2019. Cytoskeletal actin patterns shape mast cell activation. *Communications Biology* **2**:93. DOI: <https://doi.org/10.1038/s42003-019-0322-9>, PMID: 30854485
- Darvin ME**, Richter H, Ahlberg S, Haag SF, Meinke MC, Le Quintrec D, Doucet O, Lademann J. 2014. Influence of sun exposure on the cutaneous collagen/elastin fibers and carotenoids: negative effects can be reduced by

- application of sunscreen. *Journal of Biophotonics* **7**:735–743. DOI: <https://doi.org/10.1002/jbio.201300171>, PMID: 24639418
- Datta R**, Alfonso-García A, Cinco R, Gratton E. 2015. Fluorescence lifetime imaging of endogenous biomarker of oxidative stress. *Scientific Reports* **5**:1–10. DOI: <https://doi.org/10.1038/srep09848>, PMID: 25993434
- Digman MA**, Caiolfa VR, Zamai M, Gratton E. 2008. The phasor approach to fluorescence lifetime imaging analysis. *Biophysical Journal* **94**:L14–L16. DOI: <https://doi.org/10.1529/biophysj.107.120154>, PMID: 17981902
- Dong B**, Almossalha LM, Stypula-Cyrus Y, Urban BE, Chandler JE, Sun C, Zhang HF, Backman V. 2016. Superresolution intrinsic fluorescence imaging of chromatin utilizing native, unmodified nucleic acids for contrast. *PNAS* **113**:9716–9721. DOI: <https://doi.org/10.1073/pnas.1602202113>, PMID: 27535934
- Dupré-Crochet S**, Erard M, Nüße O. 2013. Ros production in phagocytes: why, when, and where? *Journal of Leukocyte Biology* **94**:657–670. DOI: <https://doi.org/10.1189/jlb.1012544>, PMID: 23610146
- Elhelu MA**. 1983. The role of macrophages in immunology. *Journal of the National Medical Association* **75**:314–317 PMID: 6343621.
- Estandarte AK**, Botchway S, Lynch C, Yusuf M, Robinson I. 2016. The use of DAPI fluorescence lifetime imaging for investigating chromatin condensation in human chromosomes. *Scientific Reports* **6**:1–12. DOI: <https://doi.org/10.1038/srep31417>, PMID: 27526631
- Ferrer MF**, Thomas P, López Ortiz AO, Errasti AE, Charo N, Romanowski V, Gorgojo J, Rodriguez ME, Carrera Silva EA, Gómez RM. 2019. Junin virus triggers macrophage activation and modulates polarization according to viral strain pathogenicity. *Frontiers in Immunology* **10**:1–12. DOI: <https://doi.org/10.3389/fimmu.2019.02499>, PMID: 31695702
- Fitzpatrick TB**. 1988. The validity and practicality of sun-reactive skin types I through VI. *Archives of Dermatology* **124**:869–871. DOI: <https://doi.org/10.1001/archderm.124.6.869>, PMID: 3377516
- Forman HJ**, Torres M. 2001. Redox signaling in macrophages. *Molecular Aspects of Medicine* **22**:189–216. DOI: [https://doi.org/10.1016/s0098-2997\(01\)00010-3](https://doi.org/10.1016/s0098-2997(01)00010-3), PMID: 11679166
- Fukui S**, Iwamoto N, Takatani A, Igawa T, Shimizu T, Umeda M, Nishino A, Horai Y, Hirai Y, Koga T, Kawashiri SY, Tamai M, Ichinose K, Nakamura H, Origuchi T, Masuyama R, Kosai K, Yanagihara K, Kawakami A. 2018. M1 and M2 monocytes in rheumatoid arthritis: a contribution of imbalance of M1/M2 monocytes to osteoclastogenesis. *Frontiers in Immunology* **8**:1–10. DOI: <https://doi.org/10.3389/fimmu.2017.01958>, PMID: 29375576
- Furukawa S**, Moriyama M, Miyake K, Nakashima H, Tanaka A, Maehara T, Iizuka-Koga M, Tsuboi H, Hayashida JN, Ishiguro N, Yamauchi M, Sumida T, Nakamura S. 2017. Interleukin-33 produced by M2 macrophages and other immune cells contributes to Th2 immune reaction of IgG4-related disease. *Scientific Reports* **7**:1–10. DOI: <https://doi.org/10.1038/srep42413>, PMID: 28205524
- Geissmann F**, Manz MG, Jung S, Sieweke MH, Merad M, Ley K. 2010. Development of monocytes, macrophages, and dendritic cells. *Science* **327**:656–661. DOI: <https://doi.org/10.1126/science.1178331>
- Gordon S**, Taylor PR. 2005. Monocyte and macrophage heterogeneity. *Nature Reviews. Immunology* **5**:953–964. DOI: <https://doi.org/10.1038/nri1733>, PMID: 16322748
- Haka AS**, Grosheva I, Chiang E, Buxbaum AR, Baird BA, Pierini LM, Maxfield FR. 2009. Macrophages create an acidic extracellular hydrolytic compartment to digest aggregated lipoproteins. *Molecular Biology of the Cell* **20**:4932–4940. DOI: <https://doi.org/10.1091/mbc.E09-07-0559>, PMID: 19812252
- Heaster TM**, Heaton AR, Sondel PM, Skala MC. 2021. Intravital metabolic autofluorescence imaging captures macrophage heterogeneity across normal and cancerous tissue. *Frontiers in Bioengineering and Biotechnology* **9**:644648. DOI: <https://doi.org/10.3389/fbioe.2021.644648>, PMID: 33959597
- Kang K**, Hammerberg C, Meunier L, Cooper KD. 1994. CD11b+ macrophages that infiltrate human epidermis after in vivo ultraviolet exposure potently produce IL-10 and represent the major secretory source of epidermal IL-10 protein. *Journal of Immunology* **153**:5256–5264 PMID: 7963579.
- König K**. 2008. Clinical multiphoton tomography. *Journal of Biophotonics* **1**:13–23. DOI: <https://doi.org/10.1002/jbio.200710022>, PMID: 19343631
- Koo SJ**, Garg NJ. 2019. Metabolic programming of macrophage functions and pathogens control. *Redox Biology* **24**:101198. DOI: <https://doi.org/10.1016/j.redox.2019.101198>, PMID: 31048245
- Kröger M**, Scheffel J, Nikolaev VV, Shirshin EA, Siebenhaar F, Schleusener J, Lademann J, Maurer M, Darwin ME. 2020. In vivo non-invasive staining-free visualization of dermal mast cells in healthy, allergy and mastocytosis humans using two-photon fluorescence lifetime imaging. *Scientific Reports* **10**:14930. DOI: <https://doi.org/10.1038/s41598-020-71901-2>, PMID: 32913196
- Lakner PH**, Monaghan MG, Möller Y, Olayioye MA, Schenke-Layland K. 2017. Applying phasor approach analysis of multiphoton FLIM measurements to probe the metabolic activity of three-dimensional in vitro cell culture models. *Scientific Reports* **7**:42730. DOI: <https://doi.org/10.1038/srep42730>, PMID: 28211922
- Li W**, Houston KD, Houston JP. 2017. Shifts in the fluorescence lifetime of EGFP during bacterial phagocytosis measured by phase-sensitive flow cytometry. *Scientific Reports* **7**:1–11. DOI: <https://doi.org/10.1038/srep40341>, PMID: 28091553
- Li Y**, Liu TM. 2018. Discovering macrophage functions using in vivo optical imaging techniques. *Frontiers in Immunology* **9**:1–20. DOI: <https://doi.org/10.3389/fimmu.2018.00502>, PMID: 29599778
- Li Y**, He Y, Miao K, Zheng Y, Deng C, Liu TM. 2020. Imaging of macrophage mitochondria dynamics in vivo reveals cellular activation phenotype for diagnosis. *Theranostics* **10**:2897–2917. DOI: <https://doi.org/10.7150/thno.40495>, PMID: 32194843
- Malissen B**, Tamoutounour S, Henri S. 2014. The origins and functions of dendritic cells and macrophages in the skin. *Nature Reviews. Immunology* **14**:417–428. DOI: <https://doi.org/10.1038/nri3683>, PMID: 24854591

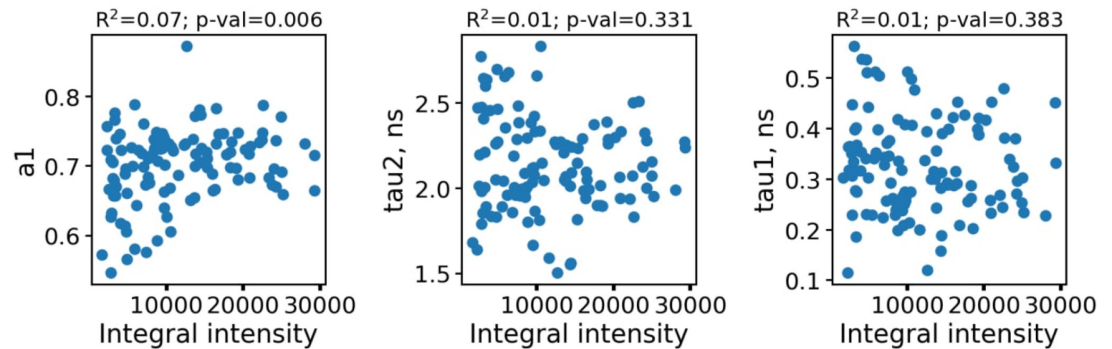
- Malmgaard L**, Melchjorsen J, Bowie AG, Mogensen SC, Paludan SR. 2004. Viral activation of macrophages through TLR-dependent and -independent pathways. *Journal of Immunology* **173**:6890–6898. DOI: <https://doi.org/10.4049/jimmunol.173.11.6890>, PMID: 15557184
- May RC**, Machesky LM. 2001. Phagocytosis and the actin cytoskeleton. *Journal of Cell Science* **114**:1061–1077. DOI: <https://doi.org/10.1242/jcs.114.6.1061>, PMID: 11228151
- McWhorter FY**, Wang T, Nguyen P, Chung T, Liu WF. 2013. Modulation of macrophage phenotype by cell shape. *PNAS* **110**:17253–17258. DOI: <https://doi.org/10.1073/pnas.1308887110>, PMID: 24101477
- Melton DW**, McManus LM, Gelfond JAL, Shireman PK. 2015. Temporal phenotypic features distinguish polarized macrophages in vitro. *Autoimmunity* **48**:161–176. DOI: <https://doi.org/10.3109/08916934.2015.1027816>, PMID: 25826285
- Mendoza-Coronel E**, Ortega E. 2017. Macrophage polarization modulates fcγR- and CD13-mediated phagocytosis and reactive oxygen species production, independently of receptor membrane expression. *Frontiers in Immunology* **8**:303. DOI: <https://doi.org/10.3389/fimmu.2017.00303>, PMID: 28396660
- Morhenn VB**, Lemperle G, Gallo RL. 2002. Phagocytosis of different particulate dermal filler substances by human macrophages and skin cells. *Dermatologic Surgery* **28**:484–490. DOI: <https://doi.org/10.1046/j.1524-4725.2002.01273.x>, PMID: 12081676
- Mosser DM**, Edwards JP. 2008. Exploring the full spectrum of macrophage activation. *Nature Reviews Immunology* **8**:958–969. DOI: <https://doi.org/10.1038/nri2448>, PMID: 19029990
- Murray PJ**, Allen JE, Biswas SK, Fisher EA, Gilroy DW, Goerdt S, Gordon S, Hamilton JA, Ivashkiv LB, Lawrence T, Locati M, Mantovani A, Martinez FO, Mege J-L, Mosser DM, Natoli G, Saeij JP, Schultze JL, Shirey KA, Sica A, et al. 2014. Macrophage activation and polarization: nomenclature and experimental guidelines. *Immunity* **41**:14–20. DOI: <https://doi.org/10.1016/j.immuni.2014.06.008>, PMID: 25035950
- Murray PJ**. 2017. Macrophage polarization. *Annual Review of Physiology* **79**:541–566. DOI: <https://doi.org/10.1146/annurev-physiol-022516-034339>, PMID: 27813830
- Myers JT**, Tsang AW, Swanson JA. 2003. Localized reactive oxygen and nitrogen intermediates inhibit escape of listeria monocytogenes from vacuoles in activated macrophages. *Journal of Immunology* **171**:5447–5453. DOI: <https://doi.org/10.4049/jimmunol.171.10.5447>, PMID: 14607950
- Nielsen MC**, Andersen MN, Møller HJ. 2020. Monocyte isolation techniques significantly impact the phenotype of both isolated monocytes and derived macrophages in vitro. *Immunology* **159**:63–74. DOI: <https://doi.org/10.1111/imm.13125>, PMID: 31573680
- Njoroge JM**, Mitchell LB, Centola M, Kastner D, Raffeld M, Miller JL. 2001. Characterization of viable autofluorescent macrophages among cultured peripheral blood mononuclear cells. *Cytometry* **44**:38–44. DOI: [https://doi.org/10.1002/1097-0320\(20010501\)44:1<38::aid-cyto1080>3.0.co;2-t](https://doi.org/10.1002/1097-0320(20010501)44:1<38::aid-cyto1080>3.0.co;2-t), PMID: 11309807
- O'Carroll C**, Fagan A, Shanahan F, Carmody RJ. 2014. Identification of a unique hybrid macrophage-polarization state following recovery from lipopolysaccharide tolerance. *Journal of Immunology* **192**:427–436. DOI: <https://doi.org/10.4049/jimmunol.1301722>, PMID: 24337373
- Orihuela R**, McPherson CA, Harry GJ. 2016. Microglial M1/M2 polarization and metabolic states. *British Journal of Pharmacology* **173**:649–665. DOI: <https://doi.org/10.1111/bph.13139>, PMID: 25800044
- Pergola C**, Schubert K, Pace S, Ziereisen J, Nikels F, Scherer O, Hüttel S, Zahler S, Vollmar AM, Weinigel C, Rummler S, Müller R, Raasch M, Mosig A, Koeberle A, Werz O. 2017. Modulation of actin dynamics as potential macrophage subtype-targeting anti-tumour strategy. *Scientific Reports* **7**:1–12. DOI: <https://doi.org/10.1038/srep41434>, PMID: 28134280
- Ploeger DT**, Hoesper NA, Schipper M, Koerts JA, de Rond S, Bank RA. 2013. Cell plasticity in wound healing: paracrine factors of M1/ M2 polarized macrophages influence the phenotypical state of dermal fibroblasts. *Cell Communication and Signaling* **11**:29. DOI: <https://doi.org/10.1186/1478-811X-11-29>, PMID: 23601247
- Porcheray F**, Viaud S, Rimaniol AC, Léone C, Samah B, Dereuddre-Bosquet N, Dormont D, Gras G. 2005. Macrophage activation switching: an asset for the resolution of inflammation. *Clinical and Experimental Immunology* **142**:481–489. DOI: <https://doi.org/10.1111/j.1365-2249.2005.02934.x>, PMID: 16297160
- Ramond E**, Jamet A, Coureuil M, Charbit A. 2019. Pivotal role of mitochondria in macrophage response to bacterial pathogens. *Frontiers in Immunology* **10**:1–11. DOI: <https://doi.org/10.3389/fimmu.2019.02461>, PMID: 31708919
- Remmerie A**, Scott CL. 2018. Macrophages and lipid metabolism. *Cellular Immunology* **330**:27–42. DOI: <https://doi.org/10.1016/j.cellimm.2018.01.020>, PMID: 29429624
- Rendra E**, Riabov V, Mossel DM, Sevastyanova T, Harmsen MC, Kzhyshkowska J. 2019. Reactive oxygen species (ROS) in macrophage activation and function in diabetes. *Immunobiology* **224**:242–253. DOI: <https://doi.org/10.1016/j.imbio.2018.11.010>, PMID: 30739804
- Ryter A**. 1985. Relationship between ultrastructure and specific functions of macrophages. *Comparative Immunology, Microbiology and Infectious Diseases* **8**:119–133. DOI: [https://doi.org/10.1016/0147-9571\(85\)90039-6](https://doi.org/10.1016/0147-9571(85)90039-6), PMID: 3910340
- Schmid MA**, Harris E. 2014. Monocyte recruitment to the dermis and differentiation to dendritic cells increases the targets for dengue virus replication. *PLOS Pathogens* **10**:e1004541. DOI: <https://doi.org/10.1371/journal.ppat.1004541>, PMID: 25474197
- Shirshin EA**, Gurfinkel YI, Priezhev AV, Fadeev VV, Lademann J, Darvin ME. 2017. Two-photon autofluorescence lifetime imaging of human skin papillary dermis in vivo: assessment of blood capillaries and structural proteins localization. *Scientific Reports* **7**:1171. DOI: <https://doi.org/10.1038/s41598-017-01238-w>, PMID: 28446767

- Shirshin EA**, Yakimov BP, Darwin ME, Omelyanenko NP, Rodionov SA, Gurfinkel YI, Lademann J, Fadeev VV, Priezzhev AV. 2019. Label-free multiphoton microscopy: the origin of fluorophores and capabilities for analyzing biochemical processes. *Biochemistry* **84**:69–88. DOI: <https://doi.org/10.1134/S0006297919140050>
- Shirshin EA**, Shirmanova MV, Gayer AV, Lukina MM, Nikonova EE, Yakimov BP, Budylin GS, Dudenkova VV, Ignatova NI, Komarov DV, Yakovlev VV, Becker W, Zagaynova EV, Shcheslavskiy VI, Scully MO. 2022. Label-free sensing of cells with fluorescence lifetime imaging: the quest for metabolic heterogeneity. *PNAS* **119**:e2118241119. DOI: <https://doi.org/10.1073/pnas.2118241119>, PMID: 35217616
- Sica A**, Mantovani A. 2012. Macrophage plasticity and polarization: in vivo veritas. *The Journal of Clinical Investigation* **122**:787–795. DOI: <https://doi.org/10.1172/JCI59643>, PMID: 22378047
- Slauch JM**. 2011. How does the oxidative burst of macrophages kill bacteria? still an open question. *Molecular Microbiology* **80**:580–583. DOI: <https://doi.org/10.1111/j.1365-2958.2011.07612.x>, PMID: 21375590
- Swindle EJ**, Hunt JA, Coleman JW. 2002. A comparison of reactive oxygen species generation by rat peritoneal macrophages and mast cells using the highly sensitive real-time chemiluminescent probe pholasin: inhibition of antigen-induced mast cell degranulation by macrophage-derived hydrogen peroxide. *Journal of Immunology* **169**:5866–5873. DOI: <https://doi.org/10.4049/jimmunol.169.10.5866>, PMID: 12421969
- Szulcowski JM**, Inman DR, Entenberg D, Ponik SM, Aguirre-Ghiso J, Castracane J, Condeelis J, Eliceiri KW, Keely PJ. 2016. In vivo visualization of stromal macrophages via label-free FLIM-based metabolite imaging. *Scientific Reports* **6**:1–9. DOI: <https://doi.org/10.1038/srep25086>, PMID: 27220760
- Teixeira J**, Basit F, Swarts HG, Forkink M, Oliveira PJ, Willems P, Koopman WJH. 2018. Extracellular acidification induces ROS- and mptp-mediated death in HEK293 cells. *Redox Biology* **15**:394–404. DOI: <https://doi.org/10.1016/j.redox.2017.12.018>, PMID: 29331741
- Theret M**, Mounier R, Rossi F. 2019. The origins and non-canonical functions of macrophages in development and regeneration. *Development* **146**:1–14. DOI: <https://doi.org/10.1242/dev.156000>, PMID: 31048317
- Trombetta AC**, Soldano S, Contini P, Tomatis V, Ruaro B, Paolino S, Brizzolara R, Montagna P, Sulli A, Pizzorni C, Smith V, Cutolo M. 2018. A circulating cell population showing both M1 and M2 monocyte/macrophage surface markers characterizes systemic sclerosis patients with lung involvement. *Respiratory Research* **19**:1–12. DOI: <https://doi.org/10.1186/s12931-018-0891-z>, PMID: 30249259
- Viola A**, Munari F, Sánchez-Rodríguez R, Scolaro T, Castegna A. 2019. The metabolic signature of macrophage responses. *Frontiers in Immunology* **10**:1–16. DOI: <https://doi.org/10.3389/fimmu.2019.01462>, PMID: 31333642
- Vogel DYS**, Heijnen PDAM, Breur M, de Vries HE, Tool ATJ, Amor S, Dijkstra CD. 2014. Macrophages migrate in an activation-dependent manner to chemokines involved in neuroinflammation. *Journal of Neuroinflammation* **11**:1–11. DOI: <https://doi.org/10.1186/1742-2094-11-23>, PMID: 24485070
- Walsh AJ**, Mueller KP, Tweed K, Jones I, Walsh CM, Piscopo NJ, Niemi NM, Pagliarini DJ, Saha K, Skala MC. 2021. Classification of T-cell activation via autofluorescence lifetime imaging. *Nature Biomedical Engineering* **5**:77–88. DOI: <https://doi.org/10.1038/s41551-020-0592-z>, PMID: 32719514
- Weber-Matthiesen K**, Sterry W. 1990. Organization of the monocyte/macrophage system of normal human skin. *The Journal of Investigative Dermatology* **95**:83–89. DOI: <https://doi.org/10.1111/1523-1747.ep12874002>, PMID: 2104511
- Xu Q**, Choksi S, Qu J, Jang J, Choe M, Banfi B, Engelhardt JF, Liu ZG. 2016. NADPH oxidases are essential for macrophage differentiation. *The Journal of Biological Chemistry* **291**:20030–20041. DOI: <https://doi.org/10.1074/jbc.M116.731216>, PMID: 27489105
- Yakimov BP**, Gogoleva MA, Semenov AN, Rodionov SA, Novoselova MV, Gayer AV, Kovalev AV, Bernakevich AI, Fadeev VV, Armaganov AG, Drachev VP, Gorin DA, Darwin ME, Shcheslavskiy VI, Budylin GS, Priezzhev AV, Shirshin EA. 2019. Label-free characterization of white blood cells using fluorescence lifetime imaging and flow-cytometry: molecular heterogeneity and erythrophagocytosis [invited]. *Biomedical Optics Express* **10**:4220–4236. DOI: <https://doi.org/10.1364/BOE.10.004220>, PMID: 31453006
- Yanez DA**, Lacher RK, Vidyarthi A, Colegio OR. 2017. The role of macrophages in skin homeostasis. *Pflügers Archiv* **469**:455–463. DOI: <https://doi.org/10.1007/s00424-017-1953-7>, PMID: 28233123
- Yang L**, Shami A. 2020. On hyperparameter optimization of machine learning algorithms: theory and practice. *Neurocomputing* **415**:295–316. DOI: <https://doi.org/10.1016/j.neucom.2020.07.061>
- Yuan R**, Li S, Geng H, Wang X, Guan Q, Li X, Ren C, Yuan X. 2017. Reversing the polarization of tumor-associated macrophages inhibits tumor metastasis. *International Immunopharmacology* **49**:30–37. DOI: <https://doi.org/10.1016/j.intimp.2017.05.014>, PMID: 28550732
- Zhang XM**, Lund H, Mia S, Parsa R, Harris RA. 2014. Adoptive transfer of cytokine-induced immunomodulatory adult microglia attenuates experimental autoimmune encephalomyelitis in DBA/1 mice. *Glia* **62**:804–817. DOI: <https://doi.org/10.1002/glia.22643>, PMID: 24677019

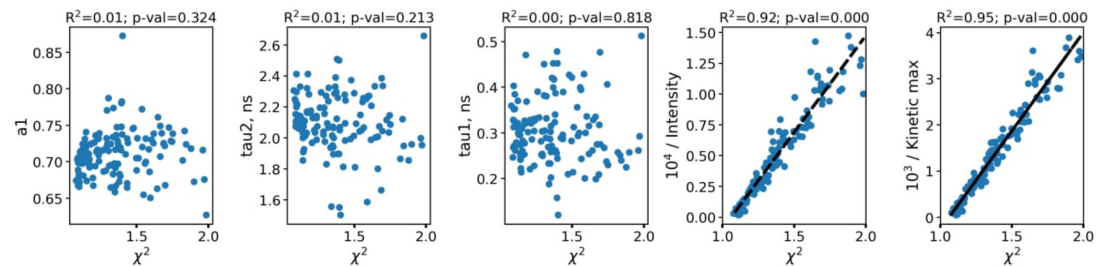
Appendix 1

FLIM data analysis

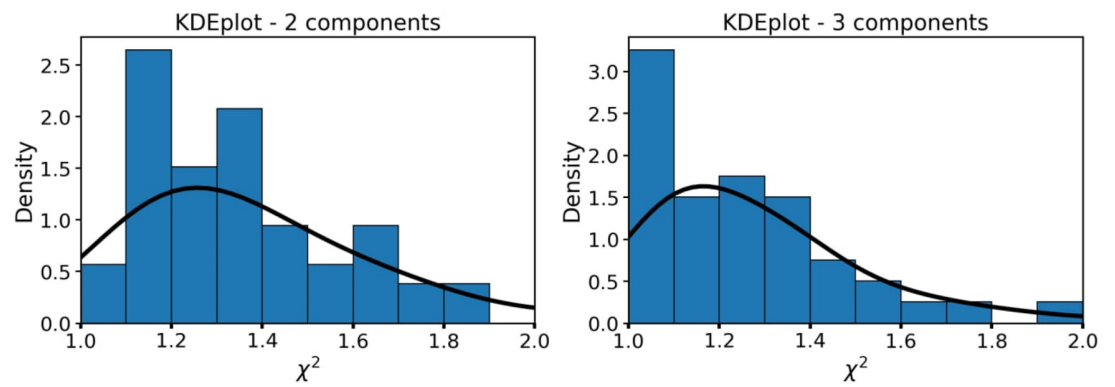
Appendix 1—figure 1 shows the dependence of fluorescence decay parameters for macrophages on the integral fluorescence intensity.



Appendix 1—figure 1. The dependence of fluorescence decay parameters for individual macrophages ($n=110$) on the integral fluorescence intensity (area under the fluorescence decay curve, upper row). As can be seen, the fluorescence decay parameters were independent on the intensity. To further confirm the absence of artefacts connected with parameters dependence on the FLIM data quality and processing algorithms, in **Appendix 1—figure 2** the dependence of fluorescence decay curves parameters on χ^2 is shown.



Appendix 1—figure 2. The dependence of fluorescence decay curves parameters on χ^2 . Each point corresponds to an individual macrophage cell ($n=110$). The dependence of χ^2 on fluorescence intensity (both integral intensity per pixel and amplitude of the fluorescence decay curve, kinetic max) is a textbook knowledge—lower signal-to-noise ratio results in a worse fitting quality and higher χ^2 . Importantly, there was no correlation between the fluorescence decay parameters obtained from the decay curves and χ^2 ; hence, there were no artefacts like lower fitting quality results in lower (or higher) values of fluorescence decay parameters. Summarizing, the fluorescence decay parameters obtained from bi-exponential fitting were independent on intensity (number of photons per pixel) and fitting quality, thus making it possible to use them as the descriptors for classification of cells. The comparison of fitting of the fluorescence decay for macrophages with two and three exponents (**Appendix 1—figure 3**). As can be seen, an increase of the number of components does not result in an increase of the fitting quality.



Appendix 1—figure 3. Distribution of the χ^2 for the bi-exponential (left) model and three-exponential (right) decay models.